NAVAL POSTGRADUATE SCHOOL

MONTEREY, CALIFORNIA

THESIS

EFFECTS OF RELATIVE PLATFORM AND TARGET MOTION ON PROPAGATION OF HIGH ENERGY LASERS

by

Hayati Emir

June 2016

Thesis Advisor: Joseph Blau
Co-Advisor: Keith Cohn

THIS PAGE INTENTIONALLY LEFT BLANK

REPORT DOCUMENTATION PAGE			*Form Approved OMB No. 0704-0188*
Public reporting burden for this collection of information is estimated to average 1 hour per response, including the time for reviewing instruction, searching existing data sources, gathering and maintaining the data needed, and completing and reviewing the collection of information. Send comments regarding this burden estimate or any other aspect of this collection of information, including suggestions for reducing this burden, to Washington headquarters Services, Directorate for Information Operations and Reports, 1215 Jefferson Davis Highway, Suite 1204, Arlington, VA 22202-4302, and to the Office of Management and Budget, Paperwork Reduction Project (0704-0188) Washington DC 20503.			
1. AGENCY USE ONLY ***(Leave blank)***	**2. REPORT DATE** June 2016	**3. REPORT TYPE AND DATES COVERED** Master's thesis	
4. TITLE AND SUBTITLE EFFECTS OF RELATIVE PLATFORM AND TARGET MOTION ON PROPAGATION OF HIGH ENERGY LASERS			**5. FUNDING NUMBERS**
6. AUTHOR(S) Hayati Emir			
7. PERFORMING ORGANIZATION NAME(S) AND ADDRESS(ES) Naval Postgraduate School Monterey, CA 93943-5000			**8. PERFORMING ORGANIZATION REPORT NUMBER**
9. SPONSORING /MONITORING AGENCY NAME(S) AND ADDRESS(ES) N/A			**10. SPONSORING / MONITORING AGENCY REPORT NUMBER**
11. SUPPLEMENTARY NOTES The views expressed in this thesis are those of the author and do not reflect the official policy or position of the Department of Defense or the U.S. Government. IRB Protocol number ____N/A____.			
12a. DISTRIBUTION / AVAILABILITY STATEMENT Approved for public release; distribution is unlimited			**12b. DISTRIBUTION CODE**

13. ABSTRACT (maximum 200 words)

To facilitate the study of engagement scenarios with high energy lasers, the Directed Energy Physics Group at the Naval Postgraduate School developed a laser performance code called Atmospheric NPS Code for HEL Optical pRopagation (ANCHOR). This code uses well-known analytical scaling laws and a scriptable user interface to allow the quick exploration of multi-dimensional parameter studies. Recently, a new capability was added that incorporates relative platform / target motion. This study demonstrates this new capability, and compares ANCHOR results with those obtained with the full diffraction code built into WaveTrain.

14. SUBJECT TERMS directed energy weapons, high energy lasers, atmospheric propagation, relative platform, target motion			**15. NUMBER OF PAGES** 83
			16. PRICE CODE
17. SECURITY CLASSIFICATION OF REPORT Unclassified	**18. SECURITY CLASSIFICATION OF THIS PAGE** Unclassified	**19. SECURITY CLASSIFICATION OF ABSTRACT** Unclassified	**20. LIMITATION OF ABSTRACT** UU

NSN 7540-01-280-5500 Standard Form 298 (Rev. 2-89)
Prescribed by ANSI Std. 239-18

THIS PAGE INTENTIONALLY LEFT BLANK

Approved for public release; distribution is unlimited

EFFECTS OF RELATIVE PLATFORM AND TARGET MOTION ON PROPAGATION OF HIGH ENERGY LASERS

Hayati Emir
Lieutenant Junior Grade, Turkish Navy
B.S., Turkish Naval Academy, 2011

Submitted in partial fulfillment of the
requirements for the degree of

MASTER OF SCIENCE IN APPLIED PHYSICS

from the

NAVAL POSTGRADUATE SCHOOL
June 2016

Approved by: Joseph Blau
Thesis Advisor

Keith Cohn
Co-Advisor

Kevin Smith
Chair, Department of Physics

THIS PAGE INTENTIONALLY LEFT BLANK

ABSTRACT

To facilitate the study of engagement scenarios with high energy lasers, the Directed Energy Physics Group at the Naval Postgraduate School developed a laser performance code called Atmospheric NPS Code for HEL Optical pRopagation (ANCHOR). This code uses well-known analytical scaling laws and a scriptable user interface to allow the quick exploration of multi-dimensional parameter studies. Recently, a new capability was added that incorporates relative platform / target motion. This study demonstrates this new capability, and compares ANCHOR results with those obtained with the full diffraction code built into WaveTrain.

THIS PAGE INTENTIONALLY LEFT BLANK

TABLE OF CONTENTS

I. INTRODUCTION....1

II. OVERVIEW OF DIRECTED ENERGY WEAPONS....3
A. HISTORY....3
B. ADVANTAGES....3
C. TECHNOLOGIES....4
1. Solid State Lasers....4
2. Free Electron Lasers....5

III. ATMOSPHERIC PROPAGATION OF HIGH ENERGY LASERS....7
A. ATMOSPHERIC EXTINCTION....7
1. Molecular Effects....7
2. Aerosol Effects....9
B. ATMOSPHERIC TURBULENCE....10
C. THERMAL BLOOMING....13

IV. METHODOLOGY....15
A. LINEAR EFFECTS ON SPOT SIZE....16
1. Beam Jitter....16
2. Diffraction....16
3. Turbulence....16
B. THE EFFECT OF THERMAL BLOOMING ON SPOT SIZE....17
1. Effective Transverse Wind Speed....20
C. OTHER PARAMETERS NEEDED TO CHARACTERIZE LASER PERFORMANCE....23
1. Power-in-the-Bucket....23
2. Dwell Time....24
a. Power Loss Mechanisms....24
b. Energy Needed to Melt the Target....25
c. Dwell Time Calculation....26
d. Laser Performance Calculation Example....26

V. RESULTS....29
A. NOTIONAL LASER/ATMOSPHERIC PARAMETERS....29
B. COMPARISON WITH WAVETRAIN....31
1. Wavetrain....31
2. Results and Discussion....31

C. ANCHOR EXAMPLES....33
1. Simple Cases....34
2. Complex Cases....37
D. PRACTICAL EXAMPLES....40
1. UAV Target....40
a. The Effect of Target Altitude and Target Speed....40
b. The Effect of Laser Output Power....43
c. The Effect of Target Direction....44
d. The Effect of Platform Velocity....45
e. The Effect of the Wind Velocity....48
2. Small Boat Target....50
a. The Effect of Target Velocity....50
b. The Effect of Laser Output Power....52
c. The Effect of Platform Velocity....53
d. The Effect of the Wind Velocity....56

VI. CONCLUSIONS....59

LIST OF REFERENCES....61

INITIAL DISTRIBUTION LIST....63

LIST OF FIGURES

Figure 1. Atmospheric transmittance measured over 1820-m horizontal path at sea level. Source: [6]. 8

Figure 2. Calculated aerosol absorption and extinction coefficients for 23-km visibility conditions and a continental aerosol model. Source: [8]. 10

Figure 3. Irradiance with weak turbulence ($C_n^2 = 10^{-18}$ $\mathrm{m}^{-2/3}$). Source: [10]. 11

Figure 4. Irradiance with moderate turbulence ($C_n^2 = 10^{-14}$ $\mathrm{m}^{-2/3}$). Source: [10]. 12

Figure 5. Irradiance with strong turbulence ($C_n^2 = 5\times10^{-14}$ $\mathrm{m}^{-2/3}$). Source: [10]. 12

Figure 6. Typical thermal blooming effected irradiance pattern with wind coming from left side ($P = 100$ kW, $R = 5$ km, $V_{wind} = 10\ \mathrm{m/s}$). Source: [10]. 14

Figure 7. Thermal blooming effected irradiance patterns with $V_{wind} = 3\ \mathrm{m/s}$ ($N_D = 465, P = 100$ kW, $R = 5$ km). Source: [10]. 18

Figure 8. Thermal blooming effected irradiance patterns with $V_{wind} = 5\ \mathrm{m/s}$ ($N_D = 279, P = 100$ kW, $R = 5$ km). Source: [10]. 19

Figure 9. Parameters used for transverse wind speed calculation. 20

Figure 10. Effective transverse wind speed for $\vec{V}_{ship} = \vec{V}_{target} = 10(\mathrm{m/s})\,\hat{y}$ and $\vec{V}_{wind} = -10(\mathrm{m/s})\,\hat{y}$ 22

Figure 11. Effective transverse wind speed for $\vec{V}_{ship} = 10(\mathrm{m/s})\,\hat{y}$, $\vec{V}_{target} = 10(\mathrm{m/s})\,\hat{x}$ and $\vec{V}_{wind} = 10(\mathrm{m/s})\hat{x} + 10(\mathrm{m/s})\hat{y}$. 23

Figure 12. Strehl ratio output comparison of Wavetrain and ANCHOR for $\vec{V}_{ship} = 10(\mathrm{m/s})\,\hat{y}$, $\vec{V}_{target} = 10(\mathrm{m/s})\,\hat{y}$, $\vec{V}_{wind} = -10(\mathrm{m/s})\,\hat{y}$, $P = 100$ kW, $\lambda = 1.064\ \mu\mathrm{m}$, $R = 5$ km and $h_T = 10$ m. Source: [10]. 32

Figure 13. Strehl ratio output comparison of Wavetrain and ANCHOR for $\vec{V}_{ship} = 10(\mathrm{m/s})\,\hat{y}$, $\vec{V}_{target} = 10(\mathrm{m/s})\,\hat{x}$, $\vec{V}_{wind} = 10(\mathrm{m/s})\hat{x} + 10(\mathrm{m/s})\hat{y}$, $P = 100$ kW, $\lambda = 1.064\ \mu\mathrm{m}$, $R = 5$ km and $h_T = 10$ m. Source: [10]. 33

Figure 14. Visualization of target orientation for $\vec{V}_{ship} = 10(\mathrm{m/s})\,\hat{y}$, $\vec{V}_{target} = 10(\mathrm{m/s})\,\hat{x}$ and $\vec{V}_{wind} = 10(\mathrm{m/s})\,\hat{x} + 10(\mathrm{m/s})\,\hat{y}$ 34

Figure 15. Simple case scenario for $\vec{V}_{wind} = -3(\mathrm{m/s})\,\hat{y}$, $h_T = 10$ m, $P = 200$ kW and $\lambda = 1.064$ μm. 35

Figure 16. Simple case scenario for $\vec{V}_{ship} = 10(\mathrm{m/s})\,\hat{y}$, $\vec{V}_{wind} = -3(\mathrm{m/s})\,\hat{y}$, $h_T = 10$ m, $P = 200$ kW and $\lambda = 1.064$ μm 35

Figure 17. Simple case scenario for $\vec{V}_{ship} = 10(\mathrm{m/s})\,\hat{y}$, $\vec{V}_{target} = 10(\mathrm{m/s})\,\hat{y}$, $\vec{V}_{wind} = -3(\mathrm{m/s})\,\hat{y}$, $h_T = 10$ m, $P = 200$ kW and $\lambda = 1.064$ μm 36

Figure 18. Simple case scenario for $\vec{V}_{ship} = 10(\mathrm{m/s})\,\hat{y}$, $\vec{V}_{target} = 55(\mathrm{m/s})\,\hat{y}$, $\vec{V}_{wind} = -3(\mathrm{m/s})\,\hat{y}$, $h_T = 10$ m, $P = 200$ kW and $\lambda = 1.064$ μm 37

Figure 19. Complex case scenario for $\vec{V}_{wind} = 2(\mathrm{m/s})\,\hat{x} - 2(\mathrm{m/s})\,\hat{y}$, $h_T = 10$ m, $P = 200$ kW and $\lambda = 1.064$ μm. 38

Figure 20. Complex case scenario for $\vec{V}_{ship} = 10(\mathrm{m/s})\,\hat{y}$, $\vec{V}_{wind} = 2(\mathrm{m/s})\,\hat{x} - 2(\mathrm{m/s})\,\hat{y}$, $h_T = 10$ m and $P = 200$ kW. 38

Figure 21. Complex case scenario for $\vec{V}_{ship} = 10(\mathrm{m/s})\,\hat{y}$, $\vec{V}_{target} = 10(\mathrm{m/s})\,\hat{x}$, $\vec{V}_{wind} = 2(\mathrm{m/s})\,\hat{x} - 2(\mathrm{m/s})\,\hat{y}$, $h_T = 10$ m, $P = 200$ kW and $\lambda = 1.064$ μm. 39

Figure 22. Complex case scenario for $\vec{V}_{ship} = 10(\mathrm{m/s})\,\hat{y}$, $\vec{V}_{target} = 55(\mathrm{m/s})\,\hat{x}$, $\vec{V}_{wind} = 2(\mathrm{m/s})\,\hat{x} - 2(\mathrm{m/s})\,\hat{y}$, $h_T = 10$ m, $P = 200$ kW and $\lambda = 1.064$ μm. 40

Figure 23. On-target irradiances for varying target velocities, $\vec{V}_{wind} = -3(\mathrm{m/s})\hat{x}$, $\vec{V}_{ship} = 2(\mathrm{m/s})\hat{x} + 2(\mathrm{m/s})\hat{y}$, $P = 200$ kW and $H_T = 300$ m. 41

Figure 24. On- target irradiances for varying target velocities, $\vec{V}_{wind} = -3(\mathrm{m/s})\hat{x}$, $\vec{V}_{ship} = 2(\mathrm{m/s})\hat{x} + 2(\mathrm{m/s})\hat{y}$, $P = 200$ kW and $H_T = 800$ m. 42

Figure 25. On-target irradiances for varying target velocities, $\vec{V}_{wind} = -3(\mathrm{m/s})\hat{x}$, $\vec{V}_{ship} = 2(\mathrm{m/s})\hat{x} + 2(\mathrm{m/s})\hat{y}$, $P = 200$ kW and $H_T = 1300$ m. 43

Figure 26. On-target irradiances for varying target velocities and laser output powers, $\vec{V}_{wind} = -3(\mathrm{m/s})\hat{x}$, $\vec{V}_{ship} = 2(\mathrm{m/s})\hat{x} + 2(\mathrm{m/s})\hat{y}$ and $H_T = 800$ m. 44

Figure 27. On-target irradiances for varying target directions and heights, $\vec{V}_{wind} = -3(\mathrm{m/s})\hat{x}$, $\vec{V}_{ship} = 2(\mathrm{m/s})\hat{x} + 2(\mathrm{m/s})\hat{y}$, $P = 200$ kW and $V_{target} = 122$ m/s. 45

Figure 28. On-target irradiances for varying target speeds and platform headıngs, $\vec{V}_{wind} = -3(\mathrm{m/s})\hat{x}$, $P = 200$ kW and $H_T = 500$ m. 46

Figure 29. On-target irradiances for varying target and platform speeds, $\vec{V}_{wind} = -3(\mathrm{m/s})\hat{x}$, $P = 200$ kW and $H_T = 500$ m. 47

Figure 30. On-target irradiances for varying wind directions and target speeds, $\vec{V}_{ship} = -9(\mathrm{m/s})\hat{x}$, $P = 200$ kW and $H_T = 800$ m. 49

Figure 31. On-target irradiances for varying wind and target speeds, $\vec{V}_{ship} = -9(\mathrm{m/s})\hat{x}$, $P = 200$ kW and $H_T = 800$ m. 50

Figure 32. On-target irradiances for varying target directions, $\vec{V}_{wind} = -3(\mathrm{m/s})\hat{x}$, $\vec{V}_{ship} = 5(\mathrm{m/s})\hat{y}$, $P = 200$ kW, $V_{target} = 9$ m/s and $H_T = 0.4$ m. 51

Figure 33. On-target irradiances for varying target velocities, $\vec{V}_{wind} = -3(\mathrm{m/s})\hat{x}$, $\vec{V}_{ship} = 5(\mathrm{m/s})\hat{y}$, $P = 200$ kW and $H_T = 0.4$ m. 52

Figure 34. On-target irradiances for varying target velocities and laser output powers, $\vec{V}_{wind} = -3(\mathrm{m/s})\hat{x}$, $\vec{V}_{ship} = 2(m/s)\hat{x} + (\mathrm{m/s})\hat{y}$ and $H_T = 0.4$ m. 53

Figure 35. On-target irradiances for varying target speeds and platform headings, $\vec{V}_{wind} = -3(\mathrm{m/s})\hat{x}$, $P = 200$ kW and $H_T = 0.4$ m. 54

Figure 36. On-target irradiances for varying target and platform speeds, $\vec{V}_{wind} = -3(\mathrm{m/s})\hat{x}$, $P = 200$ kW and $H_T = 0.4$ m. 55

Figure 37. On-target irradiances for varying target speeds and wind headings, $\vec{V}_{ship} = -3(\mathrm{m/s})\hat{x}$, $P = 200$ kW and $H_T = 0.4$ m. 57

Figure 38. On-target irradiances for varying target and wind speeds, $\vec{V}_{ship} = -3(\mathrm{m/s})\hat{x}$, $P = 200$ kW and $H_T = 0.4$ m. 58

THIS PAGE INTENTIONALLY LEFT BLANK

LIST OF TABLES

Table 1. Physical Properties of Aluminum 26

Table 2. Total Power Loss and Total Energy to Melt Calculation Results.....27

Table 3. Required On-Target Irradiances to Melt the Target Calculation Results.....27

Table 4. The Input Parameters Used in ANCHOR. 29

Table 5. Tropical Maritime Input Parameters Used for MODTRAN. 30

THIS PAGE INTENTIONALLY LEFT BLANK

LIST OF ACRONYMS AND ABBREVIATIONS

ANCHOR	Atmospheric NPS Code for High Energy Laser Optical Propagation
COAMPS	The Coupled Ocean/Atmosphere Mesoscale Prediction System
DE	directed energy
FEL	free-electron laser
HEL	high-energy laser
LEEDR	Laser Environmental Effects Definition and Reference
MODTRAN	Moderate Resolution Atmospheric Transmission
NAVSLAM	Navy Atmospheric Vertical Surface Layer Model
NPS	Naval Postgraduate School
SSL	solid-state laser

THIS PAGE INTENTIONALLY LEFT BLANK

ACKNOWLEDGMENTS

I would like to thank Professor Keith Cohn and Professor Joseph Blau for their invaluable support and advice, which really encouraged me to start and finish this thesis. Your vast knowledge in directed energy field helped me a lot finishing this thesis.

Secondly, I want to thank Dr. Conor Pogue for the hours he spent helping me willingly.

Thirdly, I want to thank to my beloved wife, Kevser, and my dear son, Poyraz, for always being by my side and believing in me.

THIS PAGE INTENTIONALLY LEFT BLANK

I. INTRODUCTION

High Energy Laser (HEL) technology has evolved to the point that laser weapons now have the capacity to be used in naval platforms. Their advantages over conventional weapons in military applications include unlimited magazines (as long as they are fed with power), low cost per shot, and very precise delivery of the payload at the speed of light.

However, unlike conventional weapons, laser weapon performance is greatly affected by weather conditions and atmospheric properties. Thus, the atmospheric propagation of HELs needs to be studied in order to characterize their effectiveness and performance as laser weapons.

In this thesis, the effects of relative target and platform motion on the atmospheric propagation of HELs is studied, in particular how this relative motion affects an atmospheric phenomenon called thermal blooming. This study is conducted by modifying a scaling code called ANCHOR that was developed by the Directed Energy Physics Group at the Naval Postgraduate School to include motions of the platform and the target. We begin this study with an overview of directed energy weapons in Chapter II. Next, we discuss the atmospheric propagation of high energy lasers in Chapter III. In Chapter IV, we discuss how the performance of the laser weapons is characterized and how the relative motion affects the atmospheric propagation. Then, we study different cases in order to investigate how the propagation is affected by the relative motion in Chapter V. Finally, we conclude our study Chapter VI.

THIS PAGE INTENTIONALLY LEFT BLANK

II. OVERVIEW OF DIRECTED ENERGY WEAPONS

A. HISTORY

Directed energy (DE) weapons are used in order to damage a target by depositing energy onto it for a specific dwell time. The most studied and promising version of directed energy weapons is lasers (light amplification by stimulated emission of radiation).

The idea of a laser started with Albert Einstein in 1916 as he predicted how stimulated emission at particular wavelengths can be achieved . The first laser, the ruby laser, was demonstrated by Ted H. Maiman in May 1960, which had around 1 watt of output power [1]. After this accomplishment, the importance of this new technology was realized and further research led to the first gas laser (He-Ne laser) demonstration in December 1960, the demonstration of the first solid-state laser (Nd:YAG) in 1964, the demonstration of the first carbon dioxide laser in 1964, and the demonstration of the first free electron laser in 1977 [1].

The technology in this area evolved to the point that laser weapons now have the capacity to be used in naval platforms. A solid state laser (SSL) weapon was tested in April 2011 on the USS *Paul Foster* (DD 964) in the Pacific Ocean, tracking and setting fire to multiple, small unmanned boat targets. The laser system was used at high power mode more than 35 times and withstood actual maritime conditions including eight-foot waves, winds of 25 knots, and fog [2].

B. ADVANTAGES

In order to understand the advantages of directed energy weapons, we need to look for the reason why they are wanted to be used in military applications and what are their capabilities that conventional weapons do not have.

The DE weapons apply damage at light speed with very good precision. The speed can overcome the target's ability to maneuver kinetic weapons, and the precision enables damage to a specific part of the target that can enhance the lethality while also

reducing the chance of collateral damage. The precision is at the level that the main beam of the Boeing Airborne Laser, a megawatt-class chemical laser, was able to hit targets that were 500 kilometers away with pinpoint accuracy [3].

Another important advantage of electric DE weapons is an essentially unlimited magazine if the platform can support the weapon with power, unlike a conventional weapon that has a specific amount of munition. This is especially important in swarm attacks where conventional weapons may be exhausted before all the targets are eliminated. Furthermore, the cost per shot for a DE weapon is cheaper than a conventional weapon. "The shipboard fuel needed to generate the electricity for firing an electrically powered laser would cost about a dollar per shot" [4]. Finally, the effects of the engagement on a target can be varied by changing the power of the DE weapon. As a result of this, nonlethal and lethal applications may be supported by a single weapon [1].

C. TECHNOLOGIES

1. Solid State Lasers

An SSL uses a solid substrate that contains dopants as a gain medium. These dopants are excited by a pumping source in order to achieve a lasing transition. A cavity that consists of two mirrors, one reflective and one partially transmittive, is used to increase the intensity of the light produced by the lasing transition via the process of stimulated emission.

Two kinds of SSLs that will potentially be used in military applications in the near term are fiber lasers and slab lasers. Slab lasers have a gain medium formed as a rectangular slab, while a fiber laser uses a long cylindrical medium consisting of an inner and an outer cladding. Fiber lasers have the advantage of easier cooling than slab lasers due to their geometry, while more light coupling can be achieved with slab lasers due to their large aspect ratio.

Since they are a more mature technology, and relatively compact compared with Free Electron Lases (FELs), SSLs are planned to be used in DE weapon applications in the near term. However, unlike FELs, they are restricted to operation at a specific wavelength, which changes with the material used as the gain medium. Also, due to the

heat produced inside the solid gain medium operation, the possibility of damaging the medium exists and limits the output power levels of SSLs. FELs do not have this problem. Also, in order to reach the desired DE application levels for SSLs, multiple lasers need to be combined, which results in a decreased beam quality and/or increased system complexity.

2. Free Electron Lasers

Free Electron Lasers (FELs) are used to harvest the energy of unbounded relativistic electrons as coherent light. There are two main types of FELs used: oscillator FELs and amplifier FELs. Either type has several core components. An injector and accelerator are the first parts, where the electron beam is created and accelerated to relativistic speed. Then these electrons pass through the undulator, where a periodically changing magnetic field forces the electrons to wiggle and emit light. In an oscillator FEL, the light is stored in a resonator and builds up over many passes. In an amplifier FEL, the light from a seed laser source is amplified over a single pass. While FELs are inefficient at extracting energy from the relativistic electrons on a single pass, the leftover energy retained in the electron beam can be very efficiently recovered to enhance the overall wall plug efficiency [1].

Since an FEL does not have a solid or gaseous gain medium, thermal effects are not as limiting a factor like other types of lasers for both beam quality and output power levels. The “basic architecture of an FEL offers a clear potential for scaling up to power levels of one or more megawatts” [4]. Oscillator FELs are not restricted to be operated at certain wavelengths, so the wavelength can be tuned to match different atmospheric transmission sweet spots. The wavelength of an amplifier FEL is fixed by the seed laser used.

FELs are typically large, expensive, and the technology used is not as mature as SSLs [1]. Another drawback of FELs is that they create harmful radiation during operation that needs to be shielded for both personnel and material safety. This may limit the use of FELs in military applications in near term, but their capability of reaching MW

power levels makes them a viable choice for the applications requiring these power levels.

III. ATMOSPHERIC PROPAGATION OF HIGH ENERGY LASERS

A. ATMOSPHERIC EXTINCTION

Light loses some of its energy along the path it transverses due to atmospheric extinction, which includes scattering and absorption.

Scattering occurs when photons interact elastically with particles in the atmosphere that results in deflection of some of the photons in arbitrary directions. "The particles responsible for scattering cover the sizes from gas molecules (~10^{-8} cm) to large raindrops and hail particles (~1 cm)" [5]. Absorption is an inelastic process in which some of the photons' energy is transferred to particles, and ultimately results in heating the atmosphere. This heating, in turn, can distort the laser beam due to thermal blooming. Thermal blooming will be discussed further in Chapter III, Section C.

The effects of scattering and absorption are quantified by Beer's Law,

$$P(\mathrm{z}) = P_0 e^{-\varepsilon z}. \tag{1}$$

In Equation (1), $P(z)$ is the laser power after traveling a distance z, P_0 represents the initial power at $z = 0$ (i.e., living the beam director) and ε represents the total extinction coefficient (in units of inverse length), which consists of absorption and scattering coefficients due to molecular and aerosol effects,

$$\varepsilon = \alpha_a + \alpha_m + \beta_a + \beta_m. \tag{2}$$

In Equation (2), α and β represent absorption and scattering coefficients, while the a and m subscripts stand for aerosol and molecular contributions, respectively. Each coefficient in Equation (2) "depends on the wavelength of the laser radiation" [6]. In order to understand absorption and scattering thoroughly, aerosol and molecular effects need to be discussed separately.

1. Molecular Effects

Since the wavelengths used in HELs are in the infrared region, so all of the effects need to be studied in this region specifically.

The atmosphere is composed of a group of gases with nearly fixed concentration and a group of gases with variable concentration [5]. Nitrogen (N_2) and oxygen (O_2) compose ~ 99 % of the atmosphere. However, they are not responsible for the absorption in near-infrared region where SSLs operate, since they are homonuclear molecules and lack dipole moments. As seen in Figure 1, water vapor (H_2O) and carbon dioxide (CO_2) are predominantly responsible for the atmospheric absorption in the infrared region. This dominance is the result of having many vibrational modes. Molecular absorption is therefore a strong function of the wavelength.

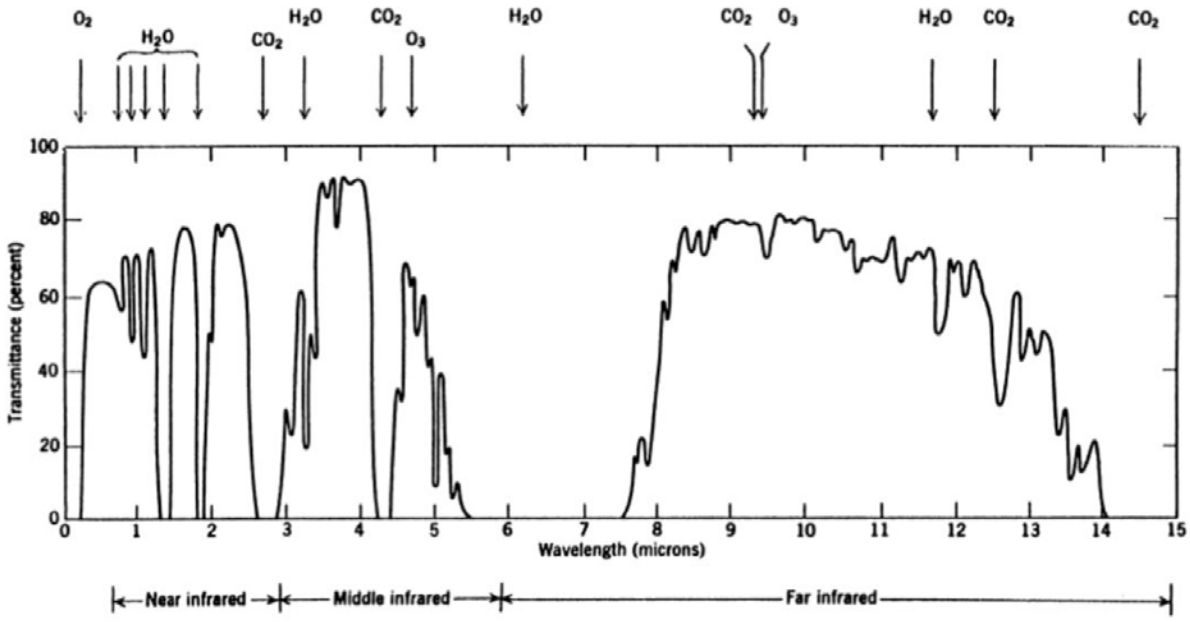

Figure 1. Atmospheric transmittance measured over 1820-m horizontal path at sea level. Source: [6].

When the wavelength of the laser is considerably larger than the particle's sizes, the scattering process is described by Rayleigh scattering. The Rayleigh scattering cross section, which is proportional to the likelihood of a scattering event occurring, can be approximated as [5]

$$\sigma_s \approx \frac{128\pi^5}{3}\frac{a^6}{\lambda^4}\left(\frac{n^2-1}{n^2+2}\right)^2, \tag{3}$$

where a is the diameter of the molecules and assumed to be much smaller than the wavelength of the laser beam $(a \ll \lambda)$, and n is the refractive index of the molecules. As wavelength increases, the effect of Rayleigh scattering on atmospheric propagation decreases rapidly $\left(\sigma_s \propto \lambda^{-4}\right)$. The sky's blue color during daytime can be explained by Rayleigh scattering; since blue light's wavelength is shorter than red light's, blue light is scattered more than red light.

Using the Rayleigh scattering cross section, the molecular scattering coefficient can be calculated as [5]

$$\beta_m(\lambda) = \sigma_s(\lambda)\int_{r_1}^{r_2} N(r)dr, \tag{4}$$

where $N(r)$ is the number density of molecules with radius r.

2. Aerosol Effects

Aerosol extinction coefficients are less dependent on the light wavelength than molecular extinction coefficients. These coefficients are determined by the combined effects of the aerosol's index of refraction and the size distribution of aerosol particles, according to the theory of Mie scattering [7]. In general, the aerosol effects are more prominent at shorter wavelengths, at least in the IR spectral region [7].

The effect of aerosol scattering on atmospheric propagation is generally far greater than molecular (Rayleigh) scattering except at very short wavelength values due to molecular scattering's dependence on wavelength as $\lambda^{-1/4}$. Figure 2 shows that for wavelengths up to $\sim 0.3\,\mu\text{m}$, molecular (Rayleigh) scattering dominates the total scattering extinction, but aerosol scattering starts to become dominant at near-IR and longer wavelengths.

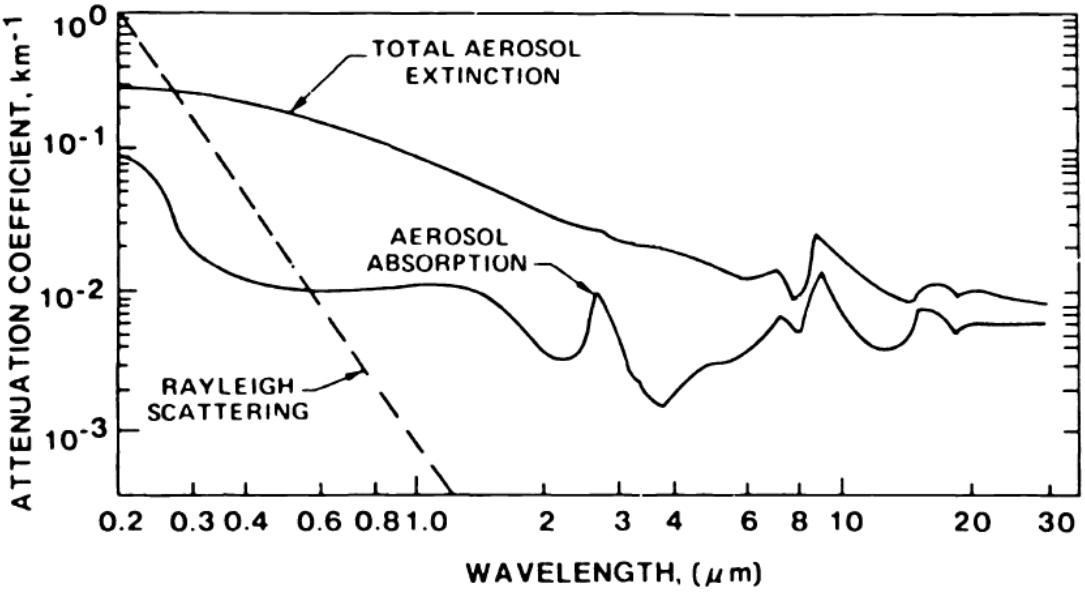

Figure 2. Calculated aerosol absorption and extinction coefficients for 23-km visibility conditions and a continental aerosol model. Source: [8].

B. ATMOSPHERIC TURBULENCE

Atmospheric turbulence is the result of temperature differences, convection, wind shear, and inertial cascades of larger scale turbulences to smaller scales [1]. Inhomogeneities in the atmosphere (eddies) result in density variations and, in turn, index of refraction differences along the laser beam path. "The shimmering of distant objects on a hot day or the twinkling of the stars at night" are examples caused by index of refraction variances due to atmospheric turbulence [9]. These index differences also distort the wave fronts of an HEL, potentially causing the laser beam to break up into beamlets that travel in slightly different directions.

An important parameter that is used to characterize the severity of atmospheric turbulence is the refractive index structure coefficient C_n^2 with units of $\mathrm{m}^{-2/3}$. This parameter increases as the temperature differences of the eddies increases, so an increase in C_n^2 means an increase in atmospheric turbulence. C_n^2 tends to decrease with altitude. Typical C_n^2 values near the surface vary from about $10^{-17}\ \mathrm{m}^{-2/3}$ for relatively weak turbulence to $10^{-13}\ \mathrm{m}^{-2/3}$ for relatively strong turbulence. Furthermore, turbulence varies

throughout the day and tends to be smallest “about one or two hours before sunrise and after sunset,” while the peak values tend to be measured around noon on sunny days [9]. The irradiance patterns for a laser propagating for 5 km through a region of constant C_n^2 are shown in Figures 3 through 5. In Figure 3, the turbulence is extremely weak at $C_n^2 = 10^{-18}$ $\mathrm{m}^{-2/3}$, which has almost no effect on the irradiance.

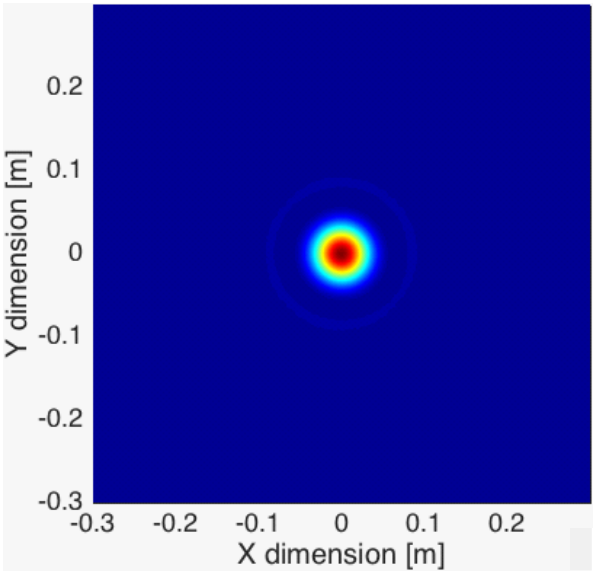

Figure 3. Irradiance with weak turbulence ($C_n^2 = 10^{-18}$ $\mathrm{m}^{-2/3}$). Source: [10].

The irradiance pattern with stronger turbulence ($C_n^2 = 10^{-14}$ $\mathrm{m}^{-2/3}$) is shown in Figure 4. The figure shows that the laser beam gets distorted as the atmospheric turbulence increases.

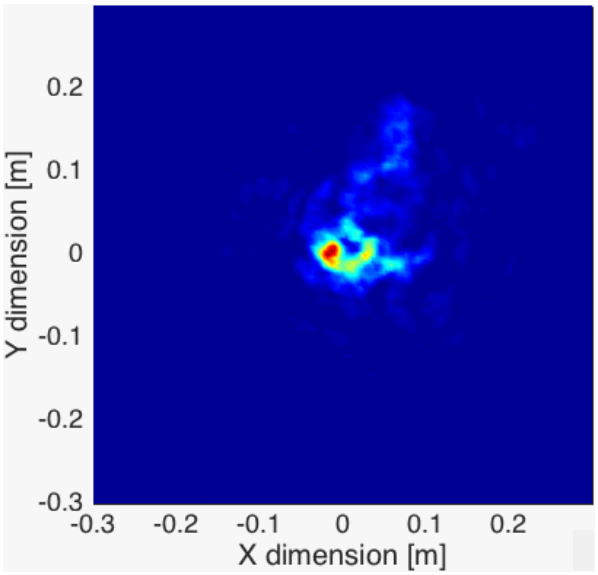

Figure 4. Irradiance with moderate turbulence ($C_n^2 = 10^{-14}$ $\mathrm{m}^{-2/3}$).
Source: [10].

The irradiance pattern with even stronger turbulence ($C_n^2 = 5\times10^{-14}$ $\mathrm{m}^{-2/3}$) is shown in Figure 5. The figure shows that the distortion level reaches to the point where the peak irradiance is down by over an order of magnitude relative to Figure 3.

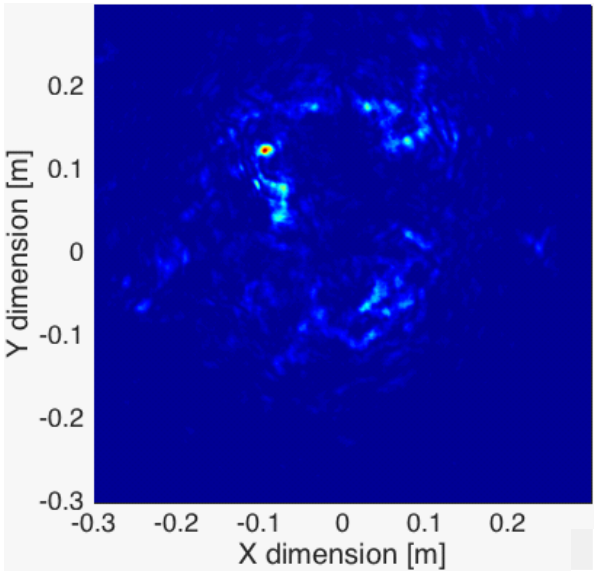

Figure 5. Irradiance with strong turbulence ($C_n^2 = 5\times10^{-14}$ $\mathrm{m}^{-2/3}$).
Source: [10].

The Fried parameter r_0 is the diameter over which transverse beam coherence is maintained. It incorporates information about C_n^2 along the path, the wavelength of the laser and the propagation distance. Larger values of r_0 correspond to weaker turbulence and more complete constructive interference at the target. For a focused beam propagating along a path of constant C_n^2, the Fried parameter is given by [1]

$$r_0 = 0.33 \frac{\lambda^{6/5}}{R^{3/5}\left(C_n^2\right)^{3/5}}, \tag{5}$$

where λ is the wavelength of the laser light and R is the range of the target. Larger C_n^2 values and longer ranges result in smaller r_0 values, while longer wavelengths result in longer r_0 values. Generally, turbulence becomes significant when r_0 is smaller than the beam director size. As an example, the Fried parameter is $r_0 \approx 12.5$ cm for $\lambda = 1$ μm, $C_n^2 = 10^{-15}$ m$^{-2/3}$ and $R = 5$ km.

C. THERMAL BLOOMING

Absorption of laser light by the molecules and aerosols in the atmosphere results in heating the air, which then changes the density of air along the laser path. These density gradients create refractive index changes in this path. These alterations in the optical properties of the path cause the air to act like a concave lens, which in turn results in defocusing and spreading of the laser beam. This nonlinear atmospheric phenomena is called thermal blooming. The effect of thermal blooming is especially crucial in low altitude engagements (due to higher water vapor and aerosol content) such as ground/sea surface-based scenarios, as well as slow moving targets in light winds due to reduced beam slewing. Wind across the beam path tends to reduce the severity of thermal blooming since it replaces the air warmed by the laser with cooler air.

There are two limiting cases of thermal blooming: conduction dominated thermal blooming and convection dominated thermal blooming [11]. Conduction-dominated thermal blooming exists for the cases where there is basically no wind ($\mathbf{v}$=0). This case is rarely met for the HEL applications along the entire beam path, though there can be

places along the path that are stagnant. Convection-dominated thermal blooming exists when there is the wind or beam motion. This case is met for most HEL applications and has been studied most extensively [11].

When wind/beam motion exists, cooler air enters from one side of the beam and warms as it transverses the beam. This causes the air to heat up in the downwind direction, and thus the refractive index drops in the downwind direction. Since light bends toward higher refractive indices, the irradiance bends into the wind, often forming a distinct crescent shape as illustrated in Figure 6.

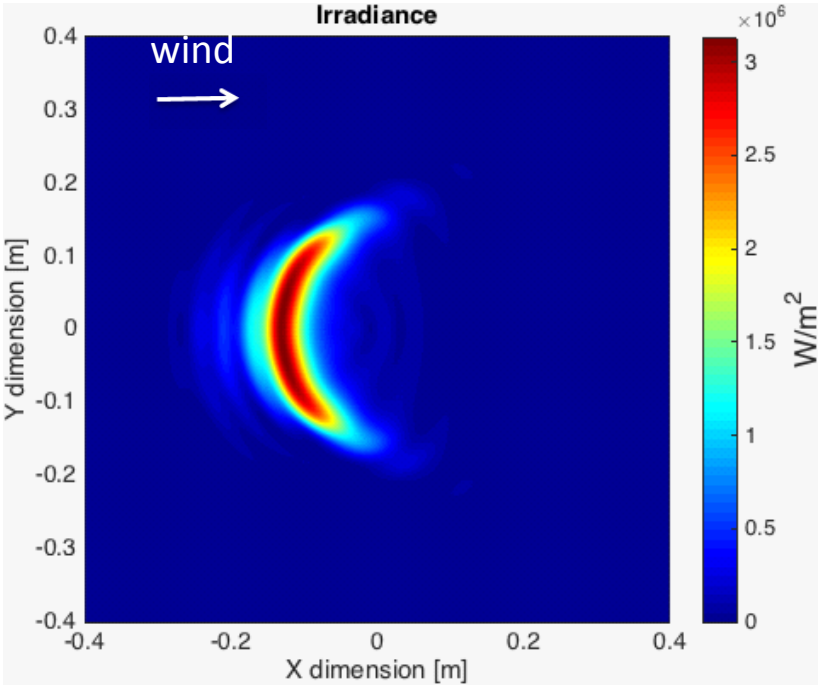

Figure 6. Typical thermal blooming effected irradiance pattern with wind coming from left side ($P = 100$ kW, $R = 5$ km, $V_{wind} = 10$ m/s). Source: [10].

IV. METHODOLOGY

ANCHOR (Atmospheric NPS Code for HEL Optical pRopagation), a scaling code developed by the NPS DE group, is used to characterize laser performance. The code incorporates parameters like turbulence, wind, jitter, and extinction. For this thesis, the effect of relative target and platform motion on atmospheric propagation was also added to the code. For different laser power and laser wavelength inputs, time averaged irradiance and power in the bucket plots can be acquired using this code. The code takes atmospheric parameters from other models like LEEDR, NAVSLAM, MODTRAN, and COAMPS.

In order to estimate the irradiance at the target, a couple of parameters need to be taken into account. Atmospheric extinction, beam quality, platform jitter, atmospheric turbulence, and thermal blooming are all effects that cause the irradiance to decrease along the propagation path. Assuming a Gaussian beam at the source, the time-averaged irradiance profile, with platform jitter and turbulence-induced wander and spreading effects included, is estimated as [7]

$$\langle I \rangle = \frac{P_{tot}}{\pi \langle w_{tot} \rangle^2} e^{-\varepsilon \ell} S_{TB}, \tag{6}$$

where P_{tot} is the total power leaves the beam director, ε is the total atmospheric extinction coefficient, ℓ is the range to the target, w_{tot} is the time-averaged $1/e$ radius of the mean irradiance profile in the absence of thermal blooming, S_{TB} represents the Strehl ratio that accounts for the effect of the thermal blooming on the time averaged irradiance. The time-averaged beam radius w_{tot} on the target is given by

$$\langle w_{tot} \rangle = \sqrt{w_j^2 + w_d^2 + w_t^2}. \tag{7}$$

In Equation (7), the j, d and t subscripts represent contributions from beam jitter, diffraction and atmospheric turbulence, respectively.

A. LINEAR EFFECTS ON SPOT SIZE

1. Beam Jitter

Beam jitter effect is caused by vibrations and/or tracking errors on the beam director platform. The time averaged mean square radial displacement of the focal spot due to beam jitter in Equation (7) is given approximately as [7]

$$w_j \approx \theta_{rms}\ell, \tag{8}$$

where θ_{rms} represents the angular variance due to jitter and ℓ is the range to the target. Typical values of angular jitter are on the order of a few μrad .

2. Diffraction

The effect of diffraction on the laser beam spot size for an infinite Gaussian source can be estimated as [7]

$$w_d = \sqrt{M^2 \frac{\ell^2}{k^2 w_0^2} + w_0^2 \left(1 - \frac{\ell}{F}\right)^2}, \tag{9}$$

where ℓ represents the range to the target, $k = 2\pi/\lambda$ is the wave number, w_0 is the $1/e$ beam radius at the beam director, F is the focal range of the laser beam, and M^2 represents the beam quality factor. The M^2 value is the measurement of how many times an ideal beam can fit across the real beam in each transverse direction at the focus. For an ideal Gaussian beam, M^2=1 whereas $M^2 > 1$ for non-ideal laser beams [12]. For this thesis, the focal range F is equal to the target range ℓ. For this condition, the second term in the square root drops out and Equation (9) simplifies to

$$w_d = \frac{M\ell}{kw_0}. \tag{10}$$

3. Turbulence

The effect of the atmospheric turbulence (see Chapter III, Section B) on the laser beam spot size can be estimated as [13]

$$w_t \approx \frac{2\ell}{kr_0}, \text{for } r_0 \le D, \tag{11}$$

where r_0 is the Fried parameter (see Equation (5)) and D represents the diameter of the beam director. The effect of atmospheric turbulence increases with the range of the target and decreases with the Fried parameter r_0 since it represents the diameter that the transverse coherence of the laser beam is maintained.

B. THE EFFECT OF THERMAL BLOOMING ON SPOT SIZE

The effect of the thermal blooming on the laser beam propagation through the atmosphere is discussed in Chapter III, Section 3. The effect on the laser beam spot size can be estimated mathematically using the thermal blooming distortion number, which is calculated as [1]

$$N_D = -\frac{4\sqrt{2}kP}{\rho_0 C_p} \int_{path} \frac{\alpha(z)\mathrm{T}(z)n_T(z)}{V_{wind}(z)D(z)}dz, \tag{12}$$

where z is the distance along the beam path, P is the initial power of the laser, ρ_0 is the ambient air density, C_p is the specific heat at constant pressure, α is the absorption coefficient, T is the transmission of the laser energy, $n_T = dn/dT = -(n_0 - 1)/T$ is the change in the refractive index of air with respect to temperature where italic T represents the temperature, V_{wind} represents the effective wind speed perpendicular to the laser beam and D is the beam diameter. Absorption near the beam director causes more significant thermal blooming distortion than the absorption near the target [1]. This effect is called lever arm effect. In order to compensate this effect, the following weighting function can be included in the integral in Equation (12) [1],

$$F(z) = \frac{1}{\sqrt{1 + \left(\frac{1.25\lambda\ell}{D^2}\right)^2 \left(\frac{z/\ell}{1 - z/\ell}\right)^2}}, \tag{13}$$

where D represents the primary aperture diameter in this case.

If there is no change in the atmospheric conditions along the path, Equation (12) can be simplified as [1]

$$N_D = \frac{-4\sqrt{2}kPn_T\alpha T}{\rho_0 C_p D V_{wind}}\ell. \tag{14}$$

Thermal blooming effects become significant when $N_D > 25$ [1]; the laser beam gets more distorted as N_D increases. In Equation (14), it is seen that the transverse effective wind decreases the distortion level due to thermal blooming, and in turn can increase the irradiance at the target. The irradiance patterns for a laser ($P = 100$ kW) propagated 5 km through a region with different effective wind speeds are shown in Figures 7 and 8. In Figure 7, the effect of the thermal blooming on irradiance is shown for $V_{wind} = 3$ m/s.

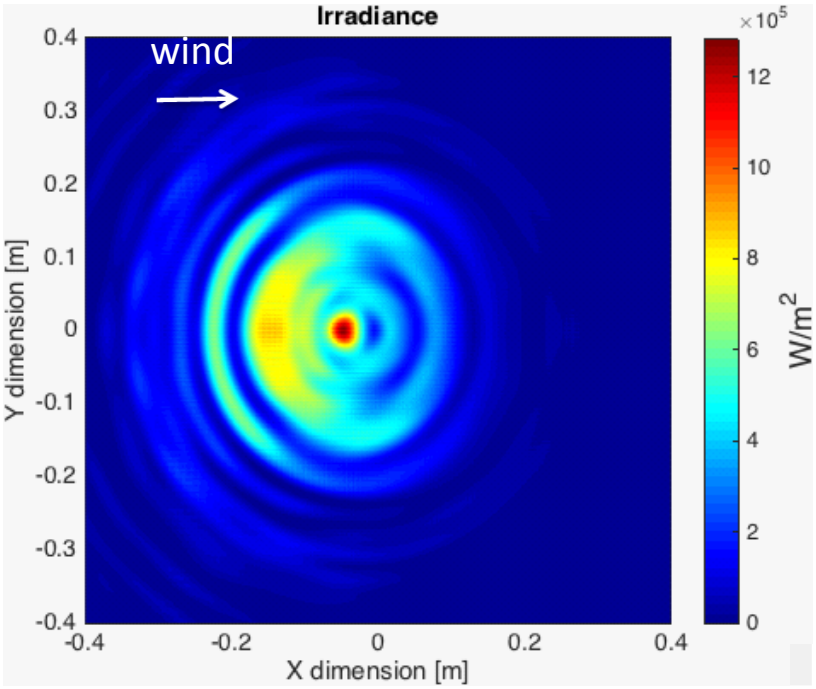

Figure 7. Thermal blooming effected irradiance patterns with $V_{wind} = 3$ m/s ($N_D = 465, P = 100$ kW, $R = 5$ km). Source: [10].

In Figure 8, the effect of the thermal blooming on irradiance is shown for $V_{wind} = 5$ m/s. It is seen that as the transverse wind speed increases, the irradiance also increases (note the different irradiance scales on the graphs), although the crescent-shaped distortion of the beam is enhanced.

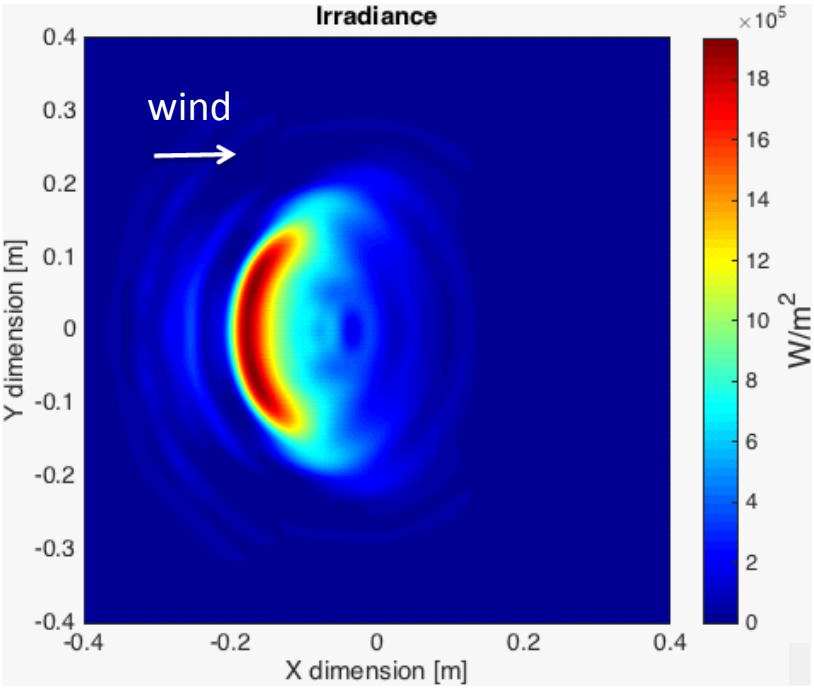

Figure 8. Thermal blooming effected irradiance patterns with $V_{wind} = 5$ m/s ($N_D = 279$, $P = 100$ kW, $R = 5$ km). Source: [10].

The Strehl ratio S_{TB}, the ratio of the peak irradiance of the thermal blooming distorted beam to the peak irradiance of a reference beam with no thermal blooming can be calculated as [1]

$$S_{TB} = \frac{I}{I_0} = \frac{1}{1 + a\left(N_D\right)^m}. \tag{15}$$

where $a = 0.0625$ and $m = 2$ for a Gaussian distributed beam, whereas $a = 0.01$ and $m = 1.2$ for a uniform distributed laser beam.

Thermal blooming also affects HEL laser systems such that after a certain laser output power, P_{crit}, the irradiance on the target starts to decrease. This critical power level can vary with the laser wavelength and the atmospheric and weather conditions, and can be estimated by [1]

$$P_{crit} = \left(\frac{P}{N_D}\right)\left(\frac{-1}{a\left(1-m\right)}\right)^{1/m}. \tag{16}$$

In ANCHOR, the distortion number from Equation (14) is calculated as well as a weighted distortion number which uses the same equation but includes a weighting function granting more effect of thermal blooming to the midpoint along the beam path. Using these two numbers, an analytic expression for the Strehl ratio is used that is calibrated against full diffraction codes.

1. Effective Transverse Wind Speed

In order to calculate the effective transverse wind speed across the beam, both target and platform motions and the natural wind need to be taken into consideration. As a result of the relative target and platform motion, the beam director must slew to keep the laser on the target. This slew motion also introduces an effective wind across the beam.

In Figure 9, the parameters needed to calculate the transverse wind speed is given. The calculations are made relative to the ship using spherical coordinates.

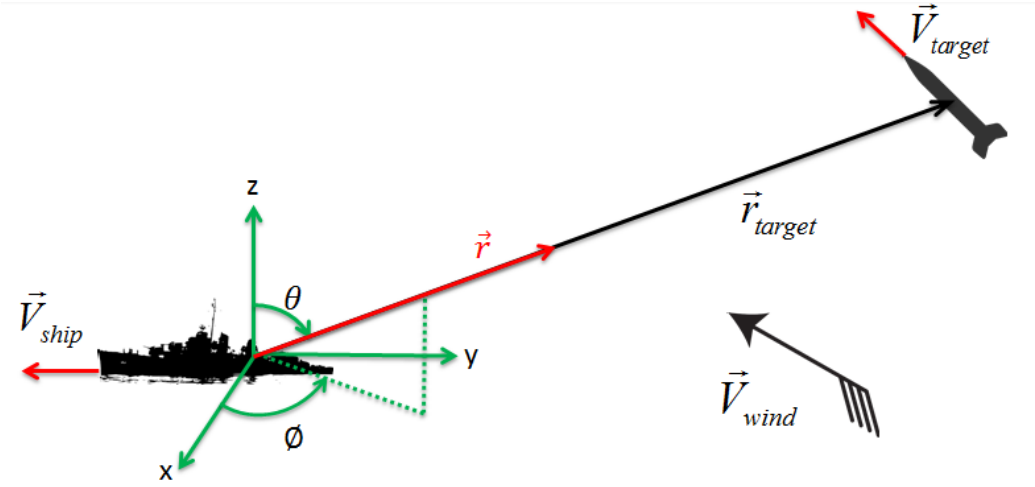

Figure 9. Parameters used for transverse wind speed calculation.

The target velocity relative to the ship is calculated as

$$\vec{V}'_{target} = \vec{V}_{target} - \vec{V}_{ship}, \tag{17}$$

where $\vec{V}_{target}$ represents the target velocity and $\vec{V}_{ship}$ is the velocity of the ship. Likewise, the wind velocity relative to the ship is calculated as

$$\vec{V}'_{wind} = \vec{V}_{wind} - \vec{V}_{ship}, \tag{18}$$

where $\vec{V}_{wind}$ represents the natural wind velocity. Angular velocity of the target about the ship is calculated using the relative target velocity as

$$\vec{\omega}' = \frac{\vec{r}_{target} \times \vec{V}'_{target}}{\left|\vec{r}_{target}\right|^2}, \tag{19}$$

where $\vec{r}_{target}$ represents the displacement vector of the target relative to the ship. Slew velocity along path $\vec{r}$ is calculated using the angular velocity of the target as

$$\vec{V}'_{slew} = \vec{\omega}' \times \vec{r}. \tag{20}$$

The effective wind velocity is calculated using the slew velocity and relative wind velocity as

$$\vec{V}_{eff} = \vec{V}'_{wind} - \vec{V}'_{slew}. \tag{21}$$

Finally, the effective transverse wind (i.e., the cross wind), is calculated using the effective velocity as

$$\vec{V}_{cross} = \left(\vec{V}_{eff} \cdot \hat{\phi}\right)\hat{\phi} + \left(\vec{V}_{eff} \cdot \hat{\theta}\right)\hat{\theta}, \tag{22}$$

where $\hat{\phi}$ and $\hat{\theta}$ are the spherical unit vectors, so

$$\hat{\phi} = -\sin\phi\hat{x} + \cos\phi\hat{y}, \tag{23}$$

and

$$\hat{\theta} = \cos\theta\cos\phi\,\hat{\mathrm{x}} + \cos\theta\sin\phi\hat{y} - \sin\theta\hat{z}. \tag{24}$$

We created a MATLAB script using these equations that plots the effective transverse wind speed for a constant target range and varying orientation about a circle centered on the ship with the same $\vec{V}_{target}$, $\vec{V}_{ship}$ and $\vec{V}_{wind}$ parameters. In Figure 10, the effective transverse wind speed is plotted for $\vec{V}_{ship} = \vec{V}_{target} = 10(\mathrm{m/s})\,\hat{\mathrm{y}}$ and $\vec{V}_{wind} = -10(\mathrm{m/s})\,\hat{\mathrm{y}}$. In these figures, arrow length represents the magnitude of the cross wind along the beam. Also, the color of the arrows evolves from blue to yellow to red as the magnitude increases. In this example, there is no cross wind along the vertical axis, because in that case the wind is in the same direction as the ship and target motion, so a

stagnation zone exists in this direction. This region is where thermal blooming will be the most problematic. Along the horizontal axis, the effect of the thermal blooming on propagation is the least because the strongest cross wind exists along this path.

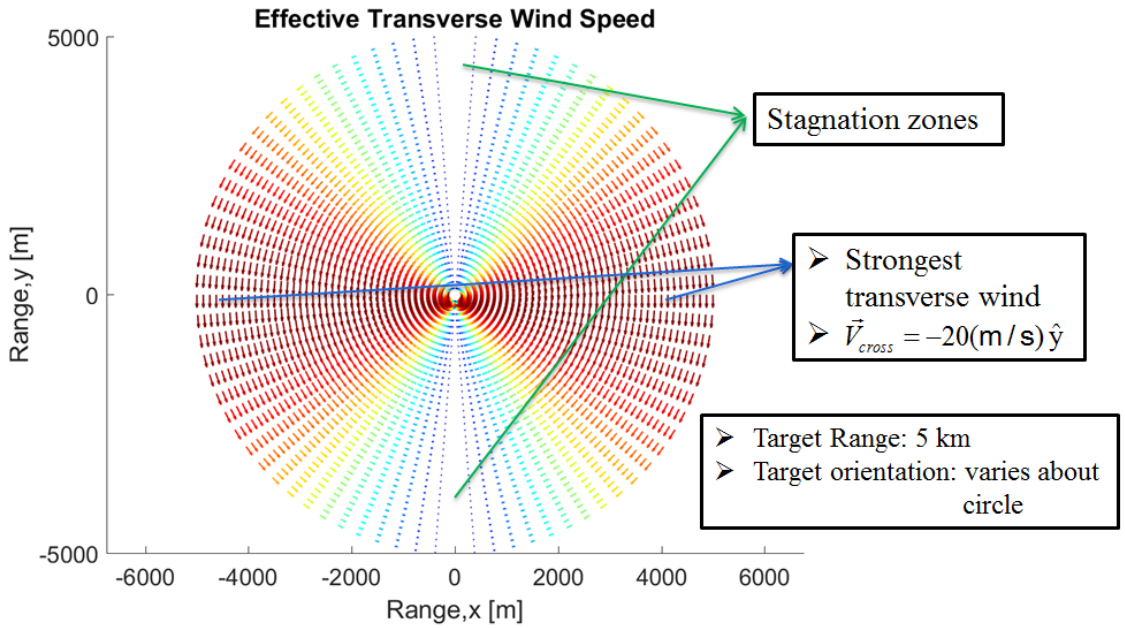

Figure 10. Effective transverse wind speed for $\vec{V}_{ship} = \vec{V}_{target} = 10(\mathrm{m/s})\,\hat{y}$ and $\vec{V}_{wind} = -10(\mathrm{m/s})\,\hat{y}$.

In Figure 11, the effective transverse wind speed is plotted for $\vec{V}_{ship} = 10(\mathrm{m/s})\,\hat{y}$, $\vec{V}_{target} = 10(\mathrm{m/s})\,\hat{x}$ and $\vec{V}_{wind} = 10(\mathrm{m/s})\hat{x} + 10(\mathrm{m/s})\hat{y}$. Here, we also see that a stagnation zone exists for certain target/ship orientations. Furthermore, the position along the path where this stagnation zone occurs changes with the orientation.

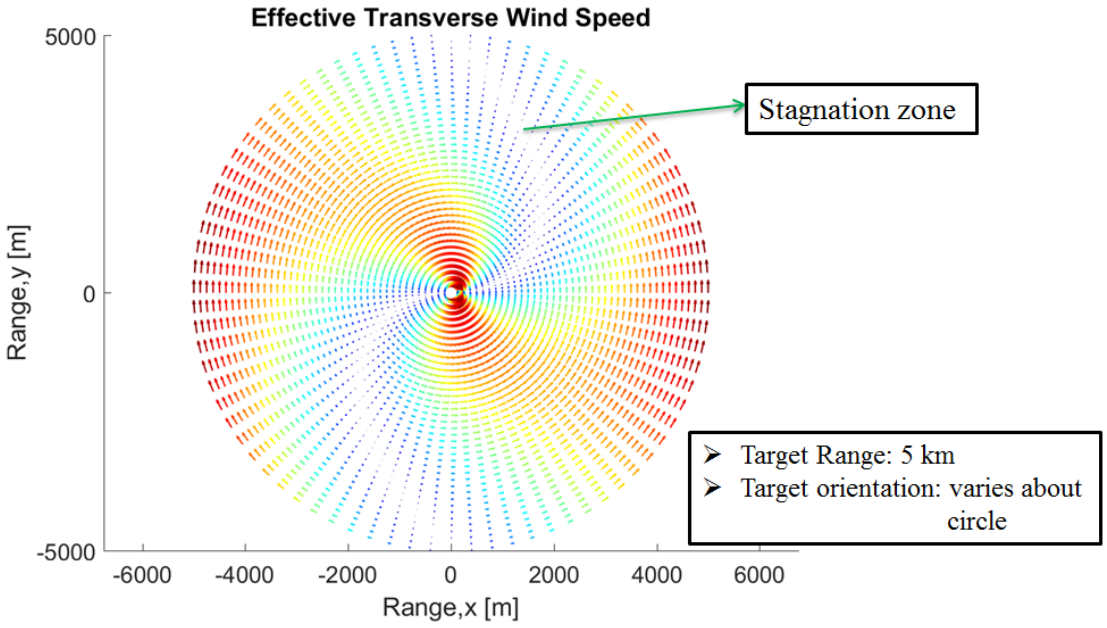

Figure 11. Effective transverse wind speed for $\vec{V}_{ship} = 10(\mathrm{m/s})\,\hat{y}$, $\vec{V}_{target} = 10(\mathrm{m/s})\,\hat{x}$ and $\vec{V}_{wind} = 10(\mathrm{m/s})\hat{x} + 10(\mathrm{m/s})\hat{y}$.

C. OTHER PARAMETERS NEEDED TO CHARACTERIZE LASER PERFORMANCE

Other than the irradiance, laser performance can be characterized by power in the bucket and dwell time.

1. Power-in-the-Bucket

The power delivered to a circle, or "bucket," of specified radius on the target is called power-in-the-bucket. The calculation of the power in the bucket changes with the chosen bucket radius r_b in comparison with the thermal blooming affected beam radius. The thermal blooming affected beam radius can be calculated using the Strehl ratio as [14]

$$w_{tot,eff}^2 = \frac{w_{tot}^2}{S_{TB}}. \tag{25}$$

Since $w_{tot,eff}$ accounts for the thermal blooming effect, the irradiance on the target can be rewritten as [14]

$$\langle I \rangle = \frac{P_{tot}}{\pi \langle w_{tot,eff} \rangle^2} e^{-\in \ell}. \tag{26}$$

If $r_b > w_{tot,eff}$, power in the bucket can be calculated approximately as [14]

$$P_B \approx \langle I \rangle \left(\pi w_{tot,eff}^2 \right) = P_{tot} e^{-\in \ell}, \tag{27}$$

as all of the delivered power falls within the defined bucket. If $r_b < w_{tot,eff}$, then the power in the bucket can be calculated approximately as [14]

$$P_B \approx \langle I \rangle \left(\pi r_b^2 \right). \tag{28}$$

In this case, we are not interested in all the power delivered to the target. The total power delivered to the target is more than the power in the bucket.

2. Dwell Time

A laser weapon is used to transfer energy to the target, and in turn damage it by melting the material used on the target. The time needed for melting through the target is called dwell time.

a. Power Loss Mechanisms

In order to calculate the dwell time, power loss on the target needs to be known. There are two power loss mechanisms: conductive and radiative losses. These losses decrease the power level transferred to the target.

Conduction loss exists as a result of the heat increase at a specific area on the target and the conduction of the heat through the other parts of the target. Conduction loss can be quantified using Fourier's heat conduction law as

$$P_{cond} = \frac{\kappa A_{cond} \left(T_m - T_0 \right)}{\Delta x}, \tag{29}$$

where κ is the thermal conductivity of the material, T_m is the melting temperature of the material, T_0 is the ambient temperature of the material, A_{cond} is the cross-sectional surface area of the surrounding material and Δx is the distance of the temperature gradient in material. This distance depends on the material properties and the dwell time;

for typical metals and dwell times of $\tau_{dwell} \sim 10$ s, $\Delta x \sim 2$ cm [15]. Typically, the conductive power loss is much greater than the radiative power loss.

Radiative power loss is due to blackbody radiation as the material heats up and glows. Using Stefan-Boltzmann law, the power radiated away is proportional to the fourth power of the blackbody's temperature ($P_{rad} \propto T^4$), the radiated power due to temperature change after laser dwell can be calculated as

$$P_{rad} = A\varepsilon\sigma(T_m^4 - T_0^4), \tag{30}$$

where A is the area over which the radiation occurs, ε is the material emissivity and σ is the Stefan-Boltzmann constant ($\sim 5.670\times10^{-8}$ $\mathrm{W\,m^{-2}\,K^{-4}}$).

Total power loss due to conduction and radiation is calculated as

$$P_{loss} = P_{cond} + P_{rad.} \tag{31}$$

The power available to melt the target can be quantified using the power loss as

$$P_{melt} = P_{trans} \times f_{target} - P_{loss,} \tag{32}$$

where P_{trans} represents the power transferred to the target and f_{target} is the fractional target absorption. For aluminum, f_{target} is ~ 0.2. In order to melt the target, the power transferred to the target must exceed the power loss on the target, otherwise the target can not be melted.

b. Energy Needed to Melt the Target

The energy needed to melt a target varies with the melting temperature of the target material, heat of fusion of the target material, and the mass of the material. The energy needed to reach the melting point of the material is calculated as

$$Q_1 = c_P m\Delta T, \tag{33}$$

where c_P represents the specific heat capacity of the material, m is the mass of the material needed to melt and $\Delta T = T_m - T_0$ is the change in the temperature. The energy needed to melt the material at the melting point is calculated as

$$Q_2 = m\Delta H, \tag{34}$$

where ΔH represents the heat of fusion of the target material. The total energy to melt the target material is calculated as

$$Q_{melt} = Q_1 + Q_2. \tag{35}$$

c. Dwell Time Calculation

Dwell time can be calculated using these calculations as

$$\tau_{dwell} = \frac{Q_{melt}}{P_{melt}}. \tag{36}$$

Dwell time can vary with the power level transferred to the target, the power loss on the target, material of the target, and the volume needed to melt.

d. Laser Performance Calculation Example

As an example, required on-target irradiances for melting a 100 cm^2 circular area on an aluminum target are calculated for dwell times of 3 and 6 seconds and material thicknesses of 1 and 3 mm. Table 1 shows the physical properties of aluminum used in these calculations.

Table 1. Physical Properties of Aluminum

Parameter	Value
Density	$2.70\ \frac{\mathrm{g}}{\mathrm{cm}^3}$
Thermal conductivity, κ	$237\ \frac{\mathrm{W}}{\mathrm{mK}}$
Distance of the temperature gradient, Δx	~ 2 cm
Melting temperature, T_m	933.47 K
Material emissivity, ε	0.05
Specific heat capacity of the material, c_P	$897\ \frac{\mathrm{J}}{\mathrm{kgK}}$
Heat of fusion of the material, ΔH	$400\ \frac{\mathrm{kJ}}{\mathrm{kg}}$

Calculated total energies to melt the target and total power losses for 1 mm and 3 mm thicknesses are shown in Table 2.

Table 2. Total Power Loss and Total Energy to Melt Calculation Results

Parameter	For 1 mm thickness	For 3 mm thickness
Total energy to melt the target, Q_{melt}	26.14 kJ	78.42 kJ
Total power loss, P_{loss}	2.68 kW	8.04 kJ

Using the parameters in Table 2, the required on-target irradiances are shown in Table 3.

Table 3. Required On-Target Irradiances to Melt the Target Calculation Results

Parameter	For 1 mm thickness	For 3 mm thickness
Required on-target irradiance to melt target for $T_D = 3$ **seconds**	$1.13 \frac{\text{MW}}{\text{m}^2}$	$3.4 \frac{\text{MW}}{\text{m}^2}$
Required on-target irradiance to melt target for $T_D = 6$ **seconds**	$0.7 \frac{\text{MW}}{\text{m}^2}$	$2.1 \frac{\text{MW}}{\text{m}^2}$

THIS PAGE INTENTIONALLY LEFT BLANK

V. RESULTS

A. NOTIONAL LASER/ATMOSPHERIC PARAMETERS

In order to evaluate the effects of relative target and platform motion on the atmospheric propagation of HELs, the parameters used as inputs to ANCHOR are given in Table 4.

Table 4. The Input Parameters Used in ANCHOR.

Laser Output Power P	200 – 1000 kW
Laser Wavelength λ	1.064 μm
Beam Quality M^2	3
Platform Height H_P	10 m Above Sea Level
Target Height H_T	0.4 – 1300 m Above Sea Level
Diameter of Beam at Source D	0.3 m
Beam Shape at Source	Uniform
Beam Jitter θ_{rms}	5×10^{-6} rad
Speed of Target V_{target}	$0 \rightarrow 198$ m/s
Speed of Platform V_{ship}	$0 \rightarrow 10$ m/s
Speed of Wind V_{wind}	$0 \rightarrow 3$ m/s
Bucket Radius r_b	0.05 m
Fractional Target Absorption	0.15

In order to evaluate the extinction coefficients for $\lambda = 1.064\ \mu m$ along the laser beam path, MODTRAN is used. MODTRAN is a commonly used radiative transfer model developed by Spectral Sciences Inc. and the U.S. Air Force Research Laboratory [16]. The parameters used as input for MODTRAN are given in Table 5.

Table 5. Tropical Maritime Input Parameters Used for MODTRAN.

Parameter	MODTRAN Model
Geographical-seasonal Model Atmosphere	Tropical atmosphere (15^{o} Latitude)
Aerosol Model	Maritime extinction
Cloud and Rain Model	No rain
Meteorological Range	23 km
Temperature, T_0	300 K at sea level (varies with altitude)
Absolute Humidity	19.7 g/m^3 (80% relative humidity) at sea level (varies with sea level)

The refractive index structure coefficient C_n^2 along the laser beam path is calculated using the Hufnagel-Valley model. This model characterizes the variations of C_n^2 with the altitude for a given surface value of C_n^2 and is specified by the following: [1]

$$C_n^2(h) = 5.94\times10^{-53}\left(\frac{W}{27}\right)^2 h^{10}e^{-h/1000} + 2.7\times10^{-16}e^{-h/1500} + Ae^{-h/100}, \qquad (37)$$

where h is the height in meters, W is the high altitude wind speed in m/s and A is the C_n^2 surface value. In this thesis, A is set to the moderate value of $10^{-14}\ \mathrm{m}^{-2/3}$.

B. COMPARISON WITH WAVETRAIN

1. Wavetrain

In order to validate the ANCHOR code results, Strehl ratio outputs are compared with the output of WaveTrain for the same conditions. WaveTrain is a software tool developed by MZA Associates Corporation "for high fidelity modeling of advanced optical systems such as laser weapons systems" [17]. It is a full diffraction code, which potentially makes it more accurate than ANCHOR, but ANCHOR is much faster than WaveTrain. All of the WaveTrain outputs for this thesis were provided by Dr. Conor Pogue.

In WaveTrain, the Strehl ratios are calculated using the same absorption coefficients, target, platform and wind velocities, target and platform heights, and target distances with ANCHOR. Strehl ratio values are the division of the peak irradiance with thermal blooming and the peak irradiance without thermal blooming for WaveTrain.

2. Results and Discussion

In Figures 12 and 13, the comparison of Strehl ratios of ANCHOR and Wavetrain is plotted in polar coordinates for a constant target range and varying orientation with the same $\vec{V}_{target}$, $\vec{V}_{ship}$ and $\vec{V}_{wind}$ parameters. Atmospheric turbulence effects are ignored for both codes. In Figure 12, the parameters used are $\vec{V}_{ship} = 10(\mathrm{m/s})\,\hat{y}$, $\vec{V}_{target} = 10(\mathrm{m/s})\,\hat{y}$, $\vec{V}_{wind} = -10(\mathrm{m/s})\,\hat{y}$, $P = 100$ kW, $\lambda = 1.064\ \mu\mathrm{m}$ (typical wavelength used in SSLs), $R = 5$ km and height of the target $h_T = 10$ m. The effective transverse wind speed plot for the same platform, target and wind velocities was shown in Figure 10. It is seen that, ANCHOR tends to underestimate the Strehl ratio more as the cross wind along the laser beam increases.

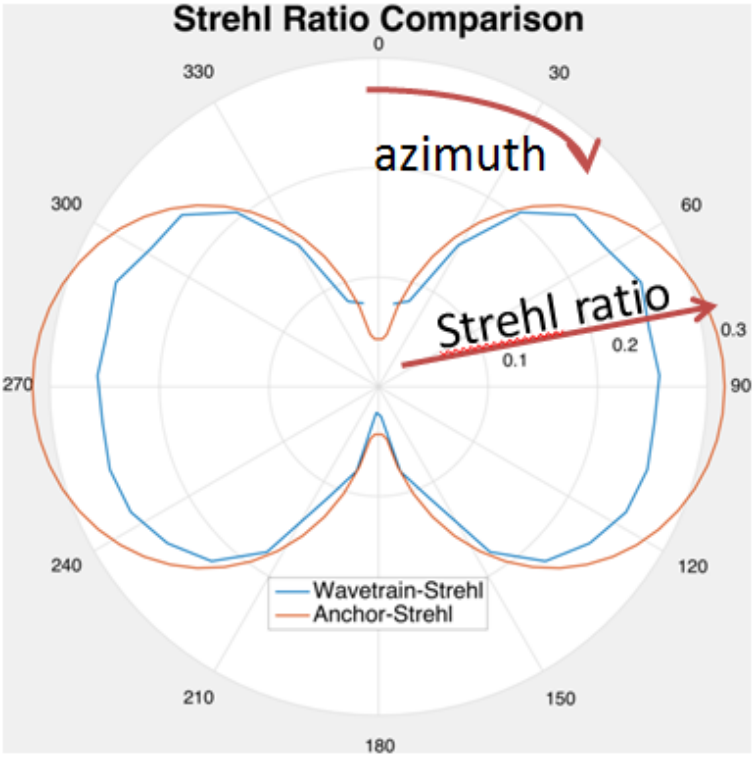

Figure 12. Strehl ratio output comparison of Wavetrain and ANCHOR for $\vec{V}_{ship} = 10(\mathrm{m/s})\,\hat{y}$, $\vec{V}_{target} = 10(\mathrm{m/s})\,\hat{y}$, $\vec{V}_{wind} = -10(\mathrm{m/s})\hat{y}$, $P = 100$ kW, $\lambda = 1.064\ \mu\mathrm{m}$, $R = 5$ km and $h_T = 10$ m. Source: [10].

In Figure 13, the parameters used are $\vec{V}_{ship} = 10(\mathrm{m/s})\,\hat{y}$, $\vec{V}_{target} = 10(\mathrm{m/s})\,\hat{x}$, $\vec{V}_{wind} = 10(\mathrm{m/s})\hat{x} + 10(\mathrm{m/s})\hat{y}$, $P = 100$ kW, $\lambda = 1.064\ \mu\mathrm{m}$, $R = 5$ km and height of the target $h_T = 10$ m. The effective transverse wind speed plot for the same platform, target and wind velocities was shown in Figure 11. It is seen that the Strehl ratios of the two methods agree generally except the regions where ANCHOR slightly underestimates the Strehl ratio in the case where the cross wind speed is larger at the zone closer to the platform and slightly overestimates the Strehl ratio where the cross wind is larger at the zone closer to the target.

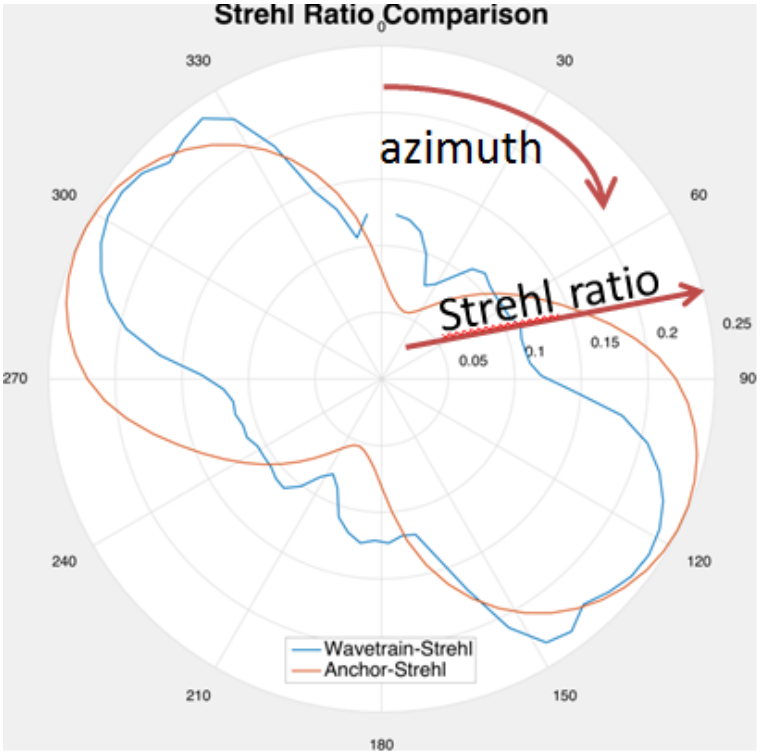

Figure 13. Strehl ratio output comparison of Wavetrain and ANCHOR for $\vec{V}_{ship} = 10(\mathrm{m/s})\,\hat{y}$, $\vec{V}_{target} = 10(\mathrm{m/s})\,\hat{x}$, $\vec{V}_{wind} = 10(\mathrm{m/s})\hat{x} + 10(\mathrm{m/s})\hat{y}$, $P = 100$ kW, $\lambda = 1.064$ μm, $R = 5$ km and $h_T = 10$ m. Source: [10].

C. ANCHOR EXAMPLES

The irradiance of the laser will be plotted for a constant target altitude, h_T, for varying target ranges from the platform at the origin. Every point except the origin corresponds to a target with the same velocity. The velocity of the wind also does not change for any target orientation. In Figure 14, these target orientations are displayed for several points on the polar plot with the velocities of $\vec{V}_{ship} = 10(\mathrm{m/s})\,\hat{y}$, $\vec{V}_{target} = 10(\mathrm{m/s})\,\hat{x}$ and $\vec{V}_{wind} = 10(\mathrm{m/s})\hat{x} + 10(\mathrm{m/s})\hat{y}$.

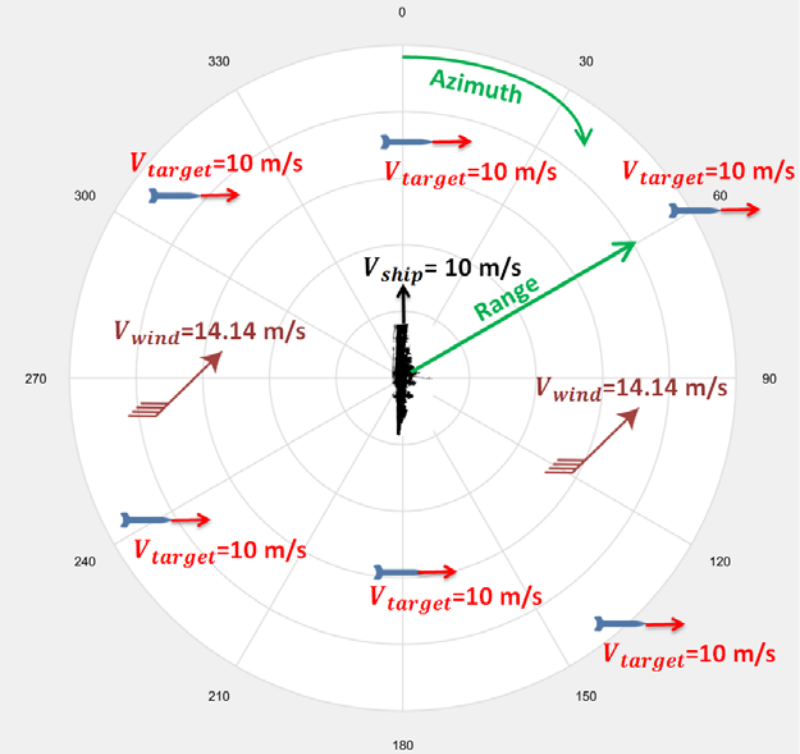

Figure 14. Visualization of target orientation for $\vec{V}_{ship} = 10(\mathrm{m/s})\,\hat{y}$, $\vec{V}_{target} = 10(\mathrm{m/s})\,\hat{x}$ and $\vec{V}_{wind} = 10(\mathrm{m/s})\,\hat{x} + 10(\mathrm{m/s})\,\hat{y}$.

1. Simple Cases

In all of the irradiance plots, latitudinal range is along the y-axis, whereas longitudinal range is along the x-axis. The contour lines on the plot connect points of constant irradiance (outer contour line is for 1 $\mathrm{MW/m^2}$, middle contour line is for 5 $\mathrm{MW/m^2}$ and inner contour line is for 10 $\mathrm{MW/m^2}$). The magnitude of the on-target irradiance is defined with the color bar scale. In Figure 15, the on-target irradiance is plotted for $\vec{V}_{wind} = -3(\mathrm{m/s})\,\hat{y}$, $h_T = 10\,\mathrm{m}$ and $P = 200\,\mathrm{kW}$. There is no relative platform and target motion for this plot. Since we have a stagnation zone on the vertical axis, and the cross wind gets stronger along the horizontal axis, we have an on-target irradiance pattern that is compressed along the vertical axis and elongated along the horizontal axis.

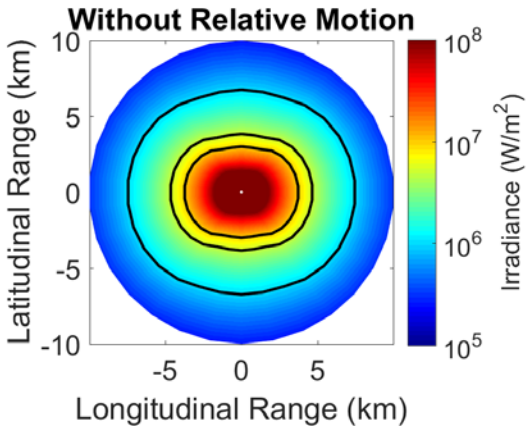

Figure 15. Simple case scenario for $\vec{V}_{wind} = -3(\mathrm{m/s})\,\hat{y}$, $h_T = 10$ m, $P = 200$ kW and $\lambda = 1.064$ μm.

In Figure 16, the on-target irradiance is plotted for $\vec{V}_{ship} = 10(\mathrm{m/s})\,\hat{y}$, $\vec{V}_{wind} = -3(\mathrm{m/s})\,\hat{y}$, $h_T = 10$ m and $P = 200$ kW. With the introduction of platform motion, the magnitude of the cross wind increases at every point except the stagnation zone for this case. The on-target irradiance also increases at every point except the stagnation zone (along the vertical axis in this case).

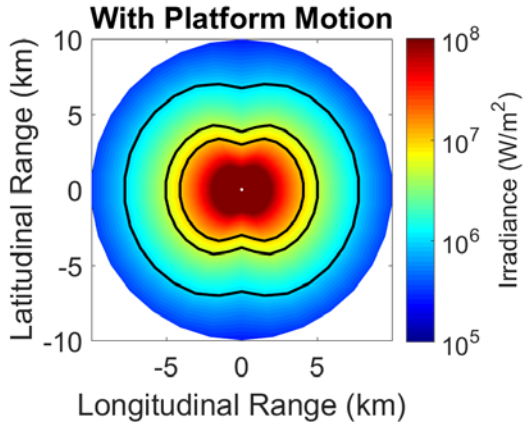

Figure 16. Simple case scenario for $\vec{V}_{ship} = 10(\mathrm{m/s})\,\hat{y}$, $\vec{V}_{wind} = -3(\mathrm{m/s})\,\hat{y}$, $h_T = 10$ m, $P = 200$ kW and $\lambda = 1.064$ μm.

In Figure 17, the on-target irradiance is plotted for $\vec{V}_{ship} = 10(\mathrm{m/s})\,\hat{y}$, $\vec{V}_{target} = 10(\mathrm{m/s})\,\hat{y}$, $\vec{V}_{wind} = -3(\mathrm{m/s})\,\hat{y}$, $h_T = 10\,\mathrm{m}$ and $P = 200\,\mathrm{kW}$. With the introduction of target motion in Figure 17, the cross wind gets stronger at every point except the stagnation zone, and in turn the irradiance increases everywhere except along this zone.

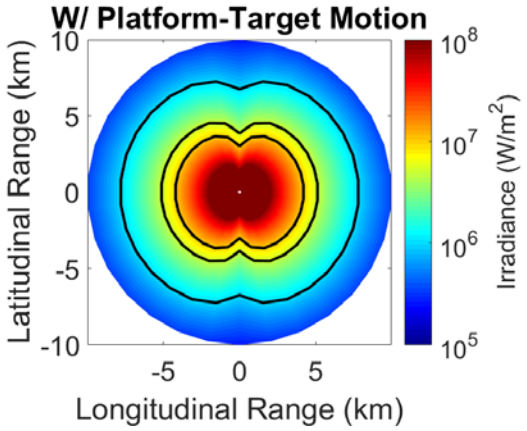

Figure 17. Simple case scenario for $\vec{V}_{ship} = 10(\mathrm{m/s})\,\hat{y}$, $\vec{V}_{target} = 10(\mathrm{m/s})\,\hat{y}$, $\vec{V}_{wind} = -3(\mathrm{m/s})\,\hat{y}$, $h_T = 10\,\mathrm{m}$, $P = 200\,\mathrm{kW}$ and $\lambda = 1.064\,\mu\mathrm{m}$.

In Figure 18, the on-target irradiance is plotted for $\vec{V}_{ship} = 10(\mathrm{m/s})\,\hat{y}$, $\vec{V}_{target} = 55(\mathrm{m/s})\,\hat{y}$, $\vec{V}_{wind} = -3(\mathrm{m/s})\,\hat{y}$, $h_T = 10\,\mathrm{m}$ and $P = 200\,\mathrm{kW}$. Since we have more target speed in this case, we also have a stronger cross wind than other simple case scenarios. As a result of this, we have the largest irradiance at every point except the stagnation zone. Since there is no change in cross wind along the stagnation zone, the irradiance at this zone stays the same for every simple case scenario.

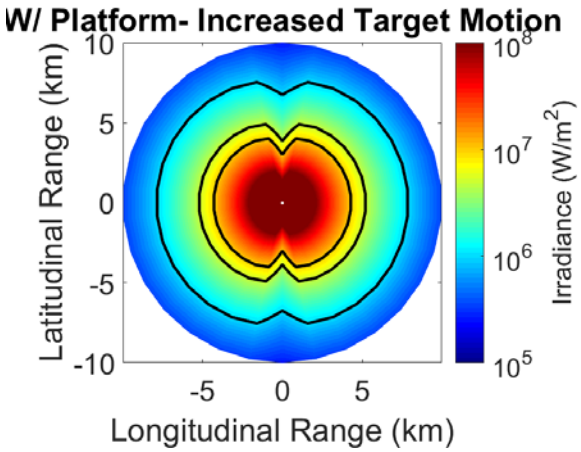

Figure 18. Simple case scenario for $\vec{V}_{ship} = 10(\text{m/s})\,\hat{y}$, $\vec{V}_{target} = 55(\text{m/s})\,\hat{y}$, $\vec{V}_{wind} = -3(\text{m/s})\,\hat{y}$, $h_T = 10\,\text{m}$, $P = 200\,\text{kW}$ and $\lambda = 1.064\,\mu\text{m}$.

2. Complex Cases

The on-target irradiances are plotted for more complex cases in this section. In Figure 19, the on-target irradiance is plotted for $\vec{V}_{wind} = 2(\text{m/s})\,\hat{x} - 2(\text{m/s})\,\hat{y}$, $h_T = 10\,\text{m}$ and $P = 200\,\text{kW}$. There is no relative platform and target motion for this plot. Since the wind blows from $315°$ azimuth, we have a stagnation zone on the line that connects $315°$ and $135°$ azimuth, whereas the cross wind gets stronger through the line that connects $45°$ and $225°$. As a result of these zones, we have a on-target irradiance pattern that is compressed along the $135°\text{-}315°$ line and elongated along the $45°\text{-}225°$ line.

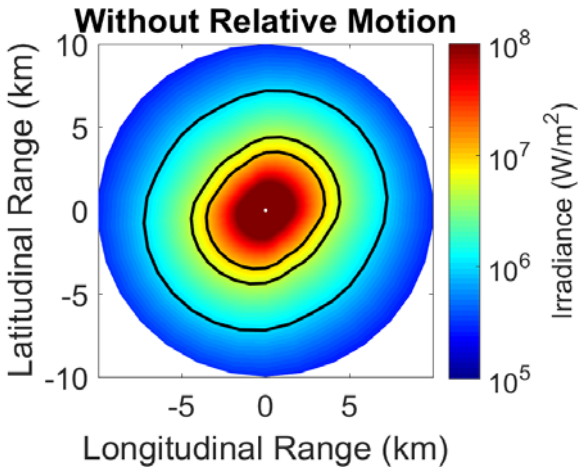

Figure 19. Complex case scenario for $\vec{V}_{wind} = 2(\text{m/s})\,\hat{x} - 2(\text{m/s})\,\hat{y}$, $h_T = 10$ m, $P = 200$ kW and $\lambda = 1.064$ μm.

In Figure 20, the on-target irradiance is plotted for $\vec{V}_{ship} = 10(\text{m/s})\,\hat{y}$, $\vec{V}_{wind} = 2(\text{m/s})\,\hat{x} - 2(\text{m/s})\,\hat{y}$, $h_T = 10$ m and $P = 200$ kW. With the introduction of relative platform and target motion, the magnitude of the effective cross wind changes at every point for this case. This results in a new orientation of the on-target irradiance pattern.

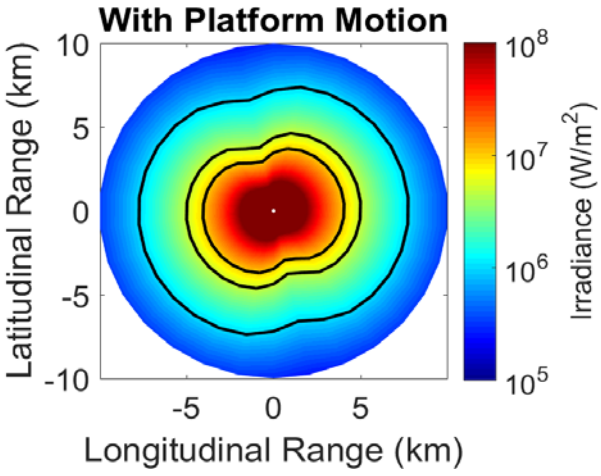

Figure 20. Complex case scenario for $\vec{V}_{ship} = 10(\text{m/s})\,\hat{y}$, $\vec{V}_{wind} = 2(\text{m/s})\,\hat{x} - 2(\text{m/s})\,\hat{y}$, $h_T = 10$ m and $P = 200$ kW.

In Figure 21, the on-target irradiance is plotted for $\vec{V}_{ship} = 10(\mathrm{m/s})\,\hat{y}$, $\vec{V}_{target} = 10(\mathrm{m/s})\,\hat{x}$, $\vec{V}_{wind} = 2(\mathrm{m/s})\,\hat{x} - 2(\mathrm{m/s})\,\hat{y}$, $h_T = 10\,\mathrm{m}$ and $P = 200\,\mathrm{kW}$. With the introduction of target motion in Figure 21, the effective cross wind changes at every point again, and in turn this results in a new on-target irradiance orientation.

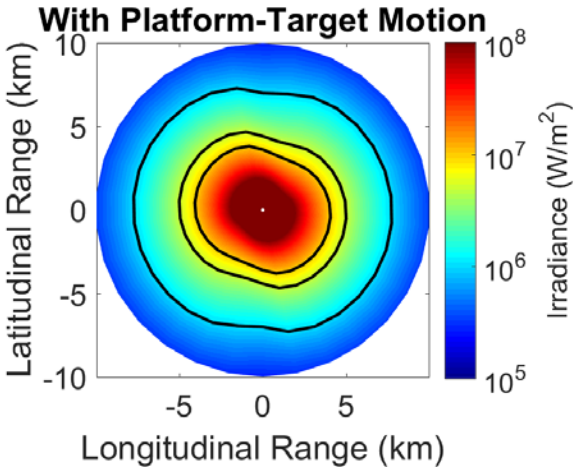

Figure 21. Complex case scenario for $\vec{V}_{ship} = 10(\mathrm{m/s})\,\hat{y}$, $\vec{V}_{target} = 10(\mathrm{m/s})\,\hat{x}$, $\vec{V}_{wind} = 2(\mathrm{m/s})\,\hat{x} - 2(\mathrm{m/s})\,\hat{y}$, $h_T = 10\,\mathrm{m}$, $P = 200\,\mathrm{kW}$ and $\lambda = 1.064\,\mu\mathrm{m}$.

In Figure 22, the on-target irradiance is plotted for $\vec{V}_{ship} = 10(\mathrm{m/s})\,\hat{y}$, $\vec{V}_{target} = 55(\mathrm{m/s})\,\hat{x}$, $\vec{V}_{wind} = 2(\mathrm{m/s})\,\hat{x} - 2(\mathrm{m/s})\,\hat{y}$, $h_T = 10\,\mathrm{m}$ and $P = 200\,\mathrm{kW}$. With the increase in target speed, both on-target irradiance magnitude and pattern orientation changes for every target position on the plot.

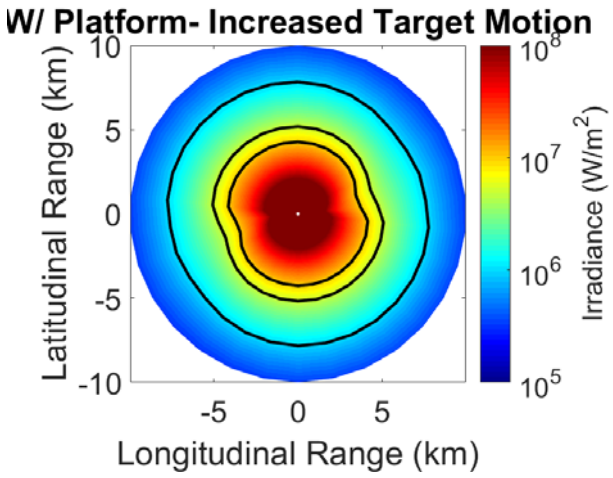

Figure 22. Complex case scenario for $\vec{V}_{ship} = 10(\mathrm{m/s})\,\hat{y}$, $\vec{V}_{target} = 55(\mathrm{m/s})\,\hat{x}$, $\vec{V}_{wind} = 2(\mathrm{m/s})\,\hat{x} - 2(\mathrm{m/s})\,\hat{y}$, $h_T = 10\,\mathrm{m}$, $P = 200\,\mathrm{kW}$ and $\lambda = 1.064\,\mu\mathrm{m}$.

D. PRACTICAL EXAMPLES

In order to characterize the effect of relative target and platform motion on the atmospheric propagation of HELs, practical examples will be evaluated via the changes in on-target irradiance for different cases in this section.

1. UAV Target

In this sub-section, the on-target irradiances will be evaluated with varying UAV velocities, varying platform (ship) velocities, varying wind velocities, different UAV altitudes and initial laser powers.

a. The Effect of Target Altitude and Target Speed

In Figures 23 through 25, the on-target irradiances are plotted for constant laser output power, wind velocity and platform velocity which are $P = 200\,\mathrm{kW}$, $\vec{V}_{wind} = -3(\mathrm{m/s})\hat{x}$ and $\vec{V}_{ship} = 2(\mathrm{m/s})\hat{x} + 2(\mathrm{m/s})\hat{y}$, respectively. Target velocities change from 20(m/s) $\hat{y}$ to 198(m/s) $\hat{y}$. In Figure 23, the on-target irradiances are plotted for target height $H_T = 300$ m. The amount that the atmospheric propagation is effected by the relative target and platform motion decreases with increasing speed of the target.

As the target speed increases, the effective cross wind starts to be dominated by the target speed, and cooling of the laser beam path leads to much less thermal blooming.

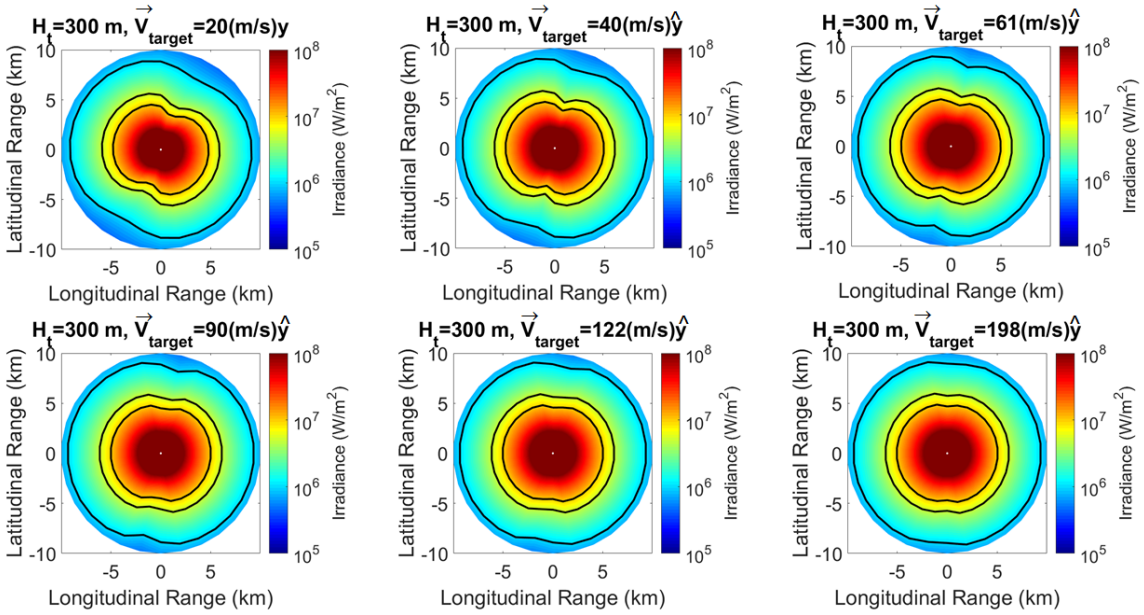

Figure 23. On-target irradiances for varying target velocities, $\vec{V}_{wind} = -3(\mathrm{m/s})\hat{x}$, $\vec{V}_{ship} = 2(\mathrm{m/s})\hat{x} + 2(\mathrm{m/s})\hat{y}$, $P = 200\,\mathrm{kW}$ and $H_T = 300\,\mathrm{m}$.

In Figure 24, the on-target irradiances are plotted for $H_T = 800$ m. The same trends are seen as in Figure 23. Also, as the target altitude increases, the slew rate of the beam director following the target decreases and in turn the effect of relative target motion decreases.

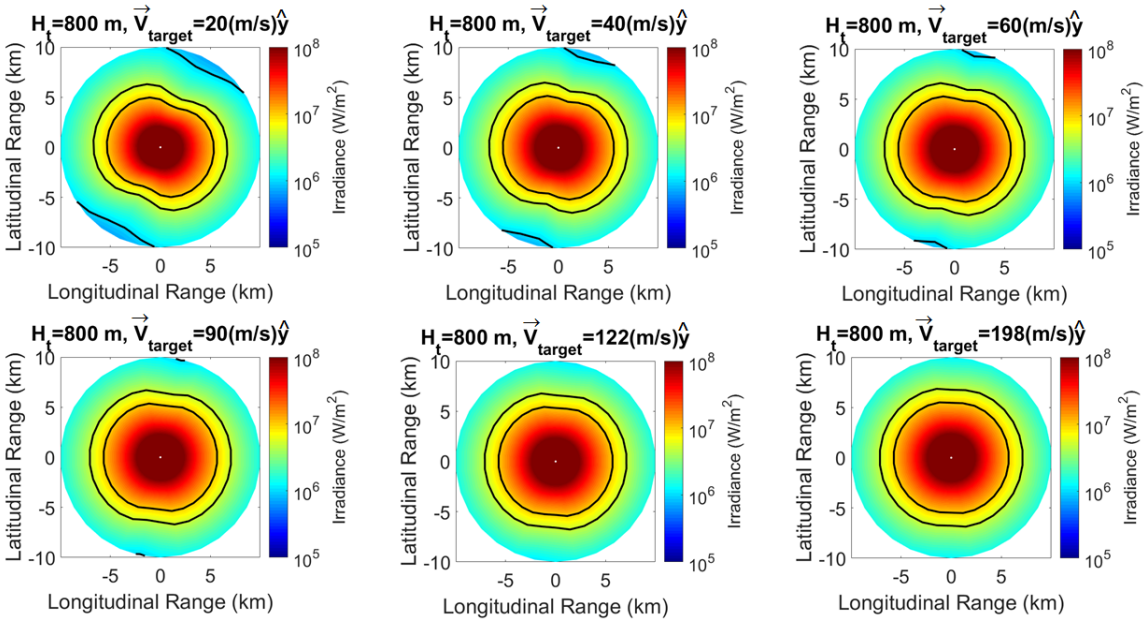

Figure 24. On- target irradiances for varying target velocities, $\vec{V}_{wind} = -3(\mathrm{m/s})\hat{x}$, $\vec{V}_{ship} = 2(\mathrm{m/s})\hat{x} + 2(\mathrm{m/s})\hat{y}$, $P = 200\,\mathrm{kW}$ and $H_T = 800\,\mathrm{m}$.

In Figure 25, the on-target irradiances are plotted for $H_T = 1300$ m. Again, the same trends are observed as in the previous figures.

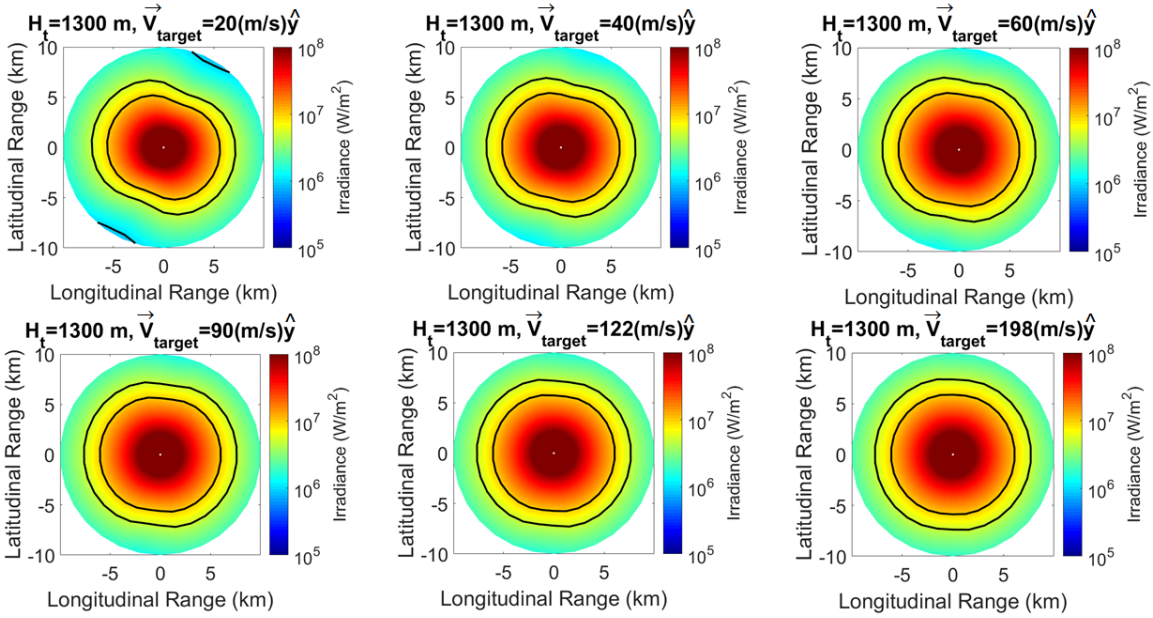

Figure 25. On-target irradiances for varying target velocities, $\vec{V}_{wind} = -3(\mathrm{m/s})\hat{x}$, $\vec{V}_{ship} = 2(\mathrm{m/s})\hat{x} + 2(\mathrm{m/s})\hat{y}$, $P = 200\,\mathrm{kW}$ and $H_T = 1300\,\mathrm{m}$.

b. The Effect of Laser Output Power

In Figure 24, the on-target irradiances are plotted for constant target heights, wind velocities, and platform velocities, which are $H_T = 800\,\mathrm{m}$, $\vec{V}_{wind} = -3(\mathrm{m/s})\hat{x}$ and $\vec{V}_{ship} = 2(\mathrm{m/s})\hat{x} + 2(\mathrm{m/s})\hat{y}$, respectively. Target velocities and laser output powers change from $20(\mathrm{m/s})\,\hat{x}$ to $60(\mathrm{m/s})\,\hat{x}$ and 200 kW to 1 MW, respectively. It is seen that the effect of the relative target and platform motion on the atmospheric propagation depends on the output laser power, since target/platform motion mainly affects thermal blooming which is more prevalent at higher laser powers.

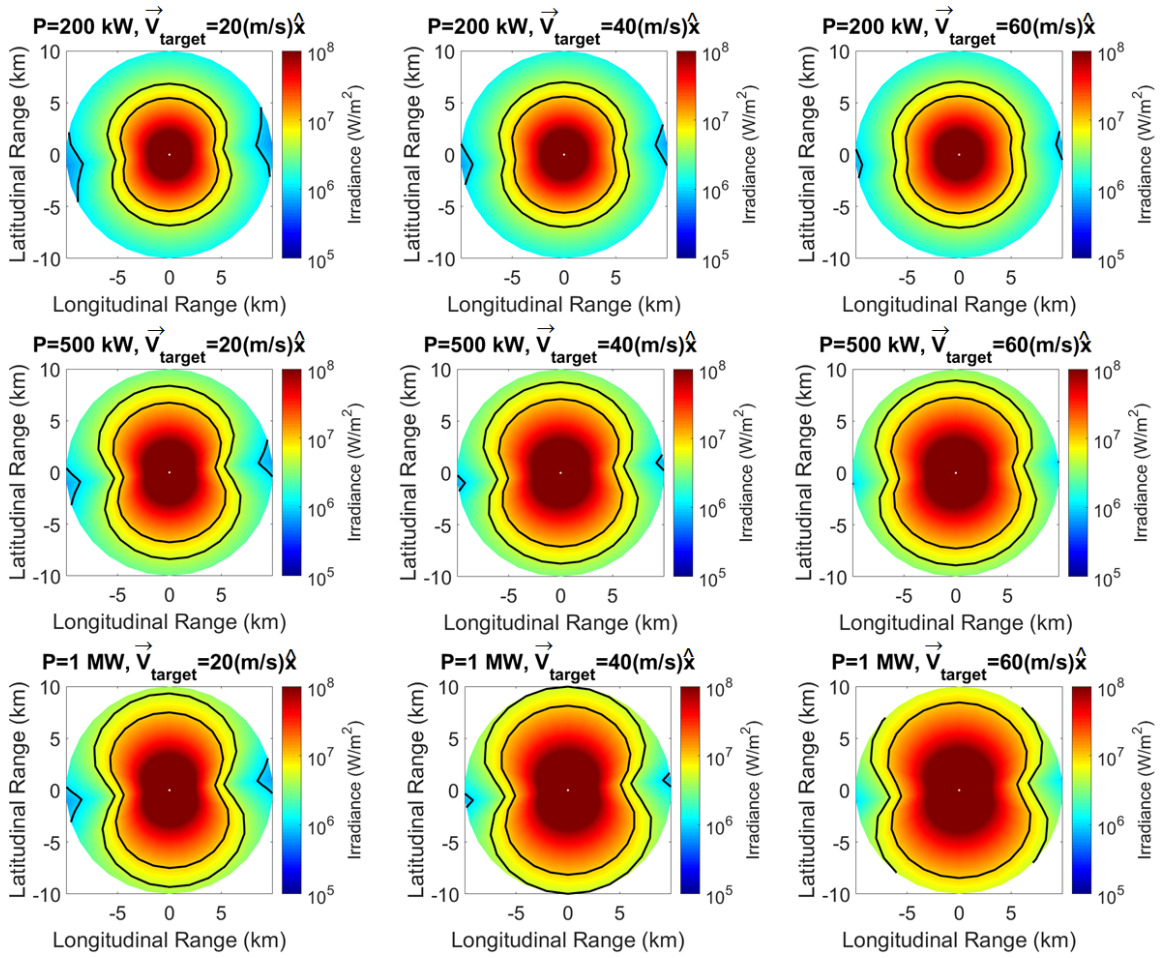

Figure 26. On-target irradiances for varying target velocities and laser output powers, $\vec{V}_{wind} = -3(\mathrm{m/s})\hat{x}$, $\vec{V}_{ship} = 2(\mathrm{m/s})\hat{x} + 2(\mathrm{m/s})\hat{y}$ and $H_T = 800\,\mathrm{m}$.

c. The Effect of Target Direction

In Figure 27, the on-target irradiances are plotted for constant laser output power, wind velocity, platform velocity, and target speed, which are $P = 200\,\mathrm{kW}$, $\vec{V}_{wind} = -3(\mathrm{m/s})\hat{x}$, $\vec{V}_{ship} = 2(\mathrm{m/s})\hat{x} + 2(\mathrm{m/s})\hat{y}$ and $V_{target} = 122$ m/s, respectively. Target direction and target altitudes change from 0° to 90° azimuth and 300 meters to 1300 meters, respectively. Figure 27 shows that the direction of the target affects the atmospheric propagation such that the orientation of the on-target irradiance contours changes in a similar manner with target heading regardless of the target height.

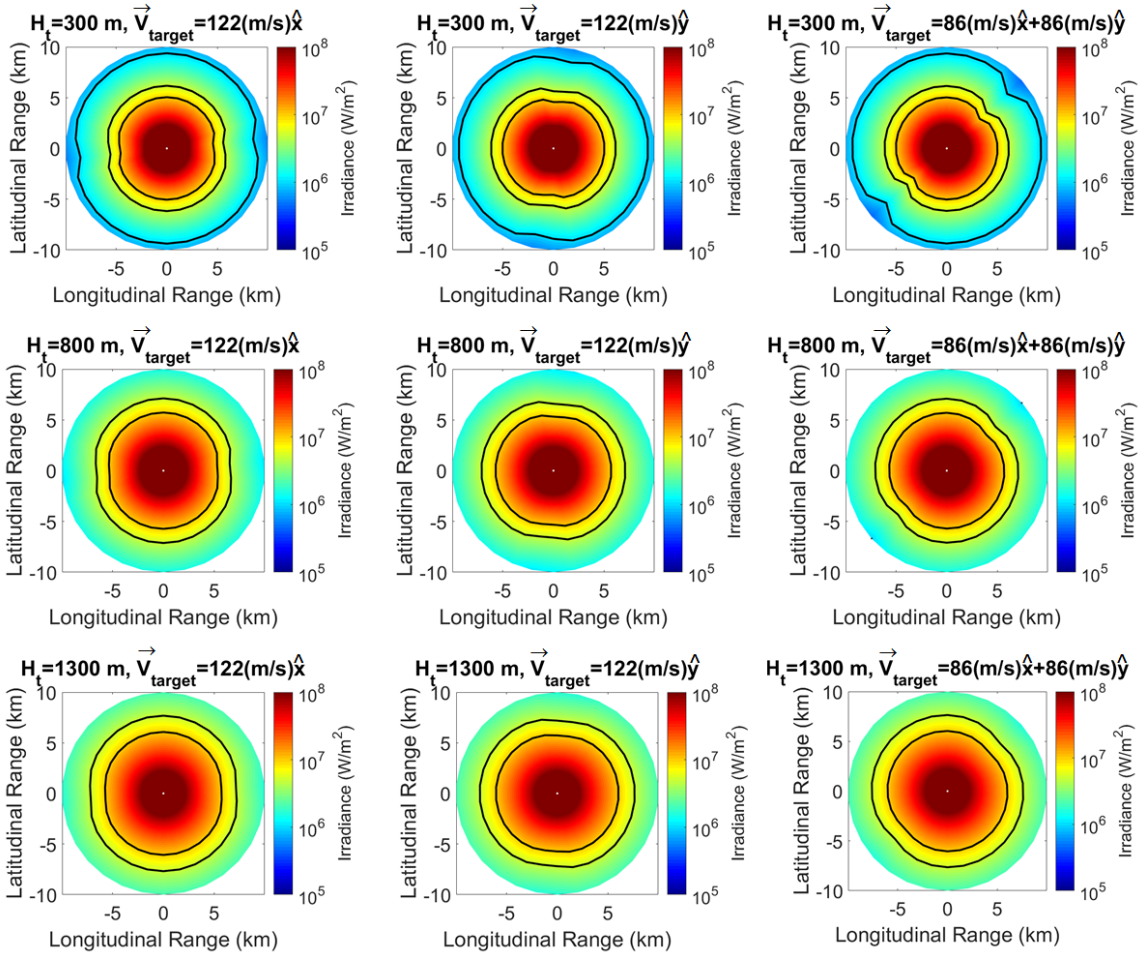

Figure 27. On-target irradiances for varying target directions and heights, $\vec{V}_{wind} = -3(\mathrm{m/s})\hat{x}$, $\vec{V}_{ship} = 2(\mathrm{m/s})\hat{x} + 2(\mathrm{m/s})\hat{y}$, $P = 200$ kW and $V_{target} = 122$ m/s.

d. The Effect of Platform Velocity

The effect of the platform velocity on the effect of relative target and platform motion on the atmospheric propagation will be studied with different platform speeds and platform headings.

(1) The Effect of Platform Direction

In Figure 28, the on-target irradiances are plotted for constant laser output power, wind velocity and target height, which are $P = 200\,\text{kW}$, $\vec{V}_{wind} = -3(\text{m/s})\hat{x}$, and $H_T = 500$ m, respectively. Target speed changes from 20 m/s to 180 m/s in the y-direction and platform direction changes but with a constant speed of 9 m/s. As the target speed increases, it starts to dominate the irradiance pattern and the platform direction has less of an impact.

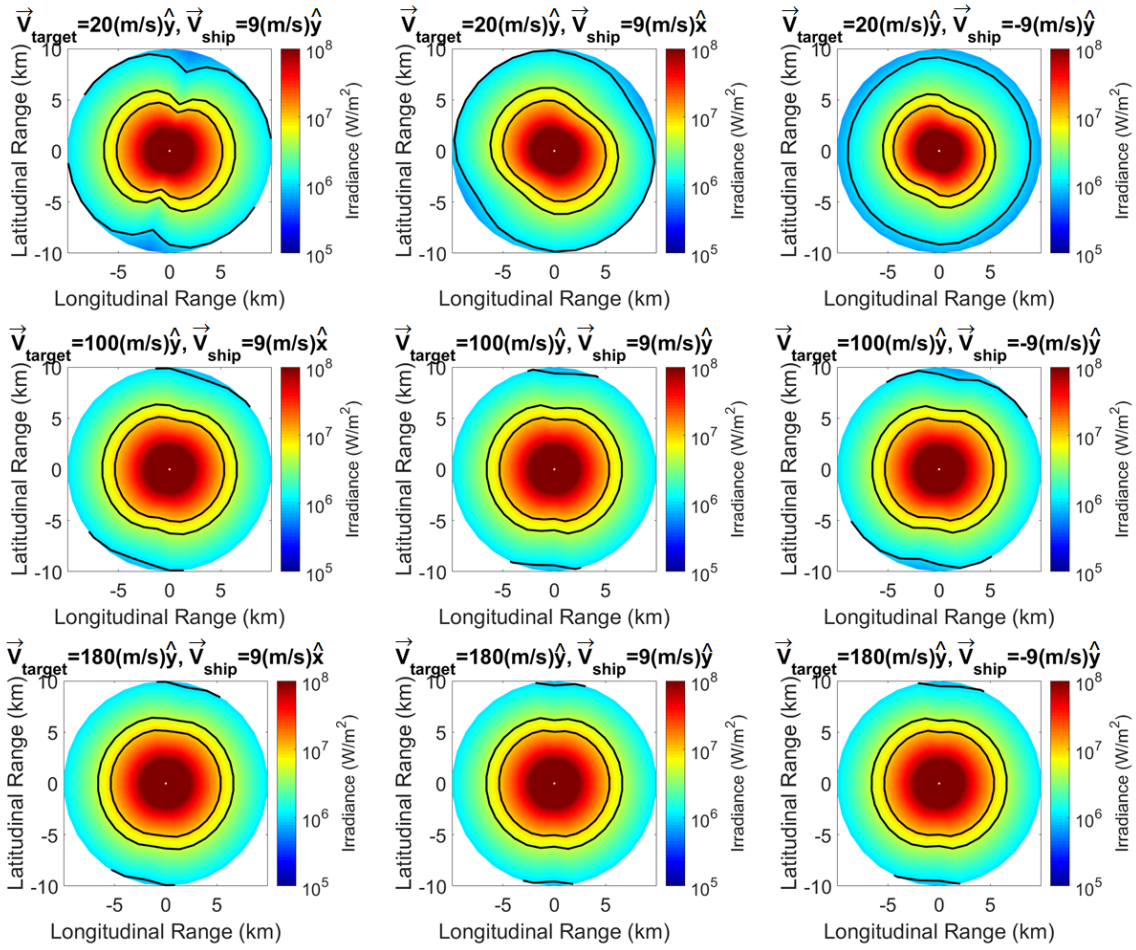

Figure 28. On-target irradiances for varying target speeds and platform headıngs, $\vec{V}_{wind} = -3(\text{m/s})\hat{x}$, $P = 200\,\text{kW}$ and $H_T = 500$ m.

(2) The Effect of Platform Speed

In Figure 29, the on-target irradiances are plotted for constant laser output power, wind velocity and target height, which are $P = 200\,\text{kW}$, $\vec{V}_{wind} = -3(\text{m/s})\hat{x}$, and $H_T = 500$ m, respectively. Target speed changes from 20 m/s to 180 m/s in the y-direction and platform speed changes from 5 m/s to 15 m/s in the x-direction. As the target speed increases, it starts to dominate the irradiance pattern and the platform speed has less of an impact.

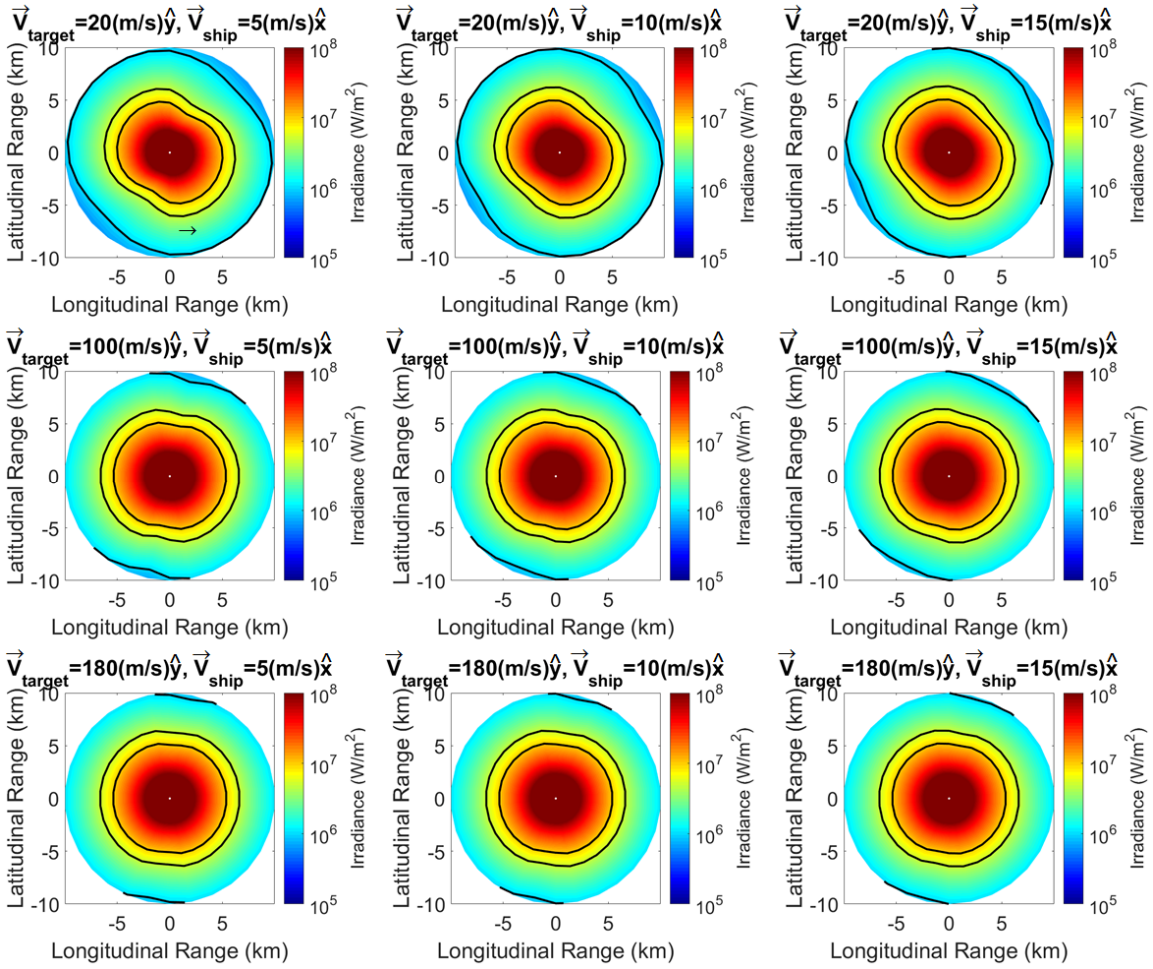

Figure 29. On-target irradiances for varying target and platform speeds, $\vec{V}_{wind} = -3(\text{m/s})\hat{x}$, $P = 200\,\text{kW}$ and $H_T = 500$ m.

e. The Effect of the Wind Velocity

The effect of the wind velocity on the effect of relative target and platform motion on the atmospheric propagation will be studied with different wind speeds and wind headings.

(1) The Effect of Wind Direction

In Figure 30, the on-target irradiances are plotted for constant laser output power, platform velocity and target height, which are $P = 200\,\text{kW}$, $\vec{V}_{ship} = -9(\text{m/s})\hat{x}$, and $H_T = 800$ m, respectively. Target speed changes from 20 m/s to 180 m/s in the y-direction and wind direction changes but with a constant speed of 4 m/s. As the target speed increases, it starts to dominate the irradiance pattern and the wind direction has less of an impact on the irradiance like the effect of platform direction.

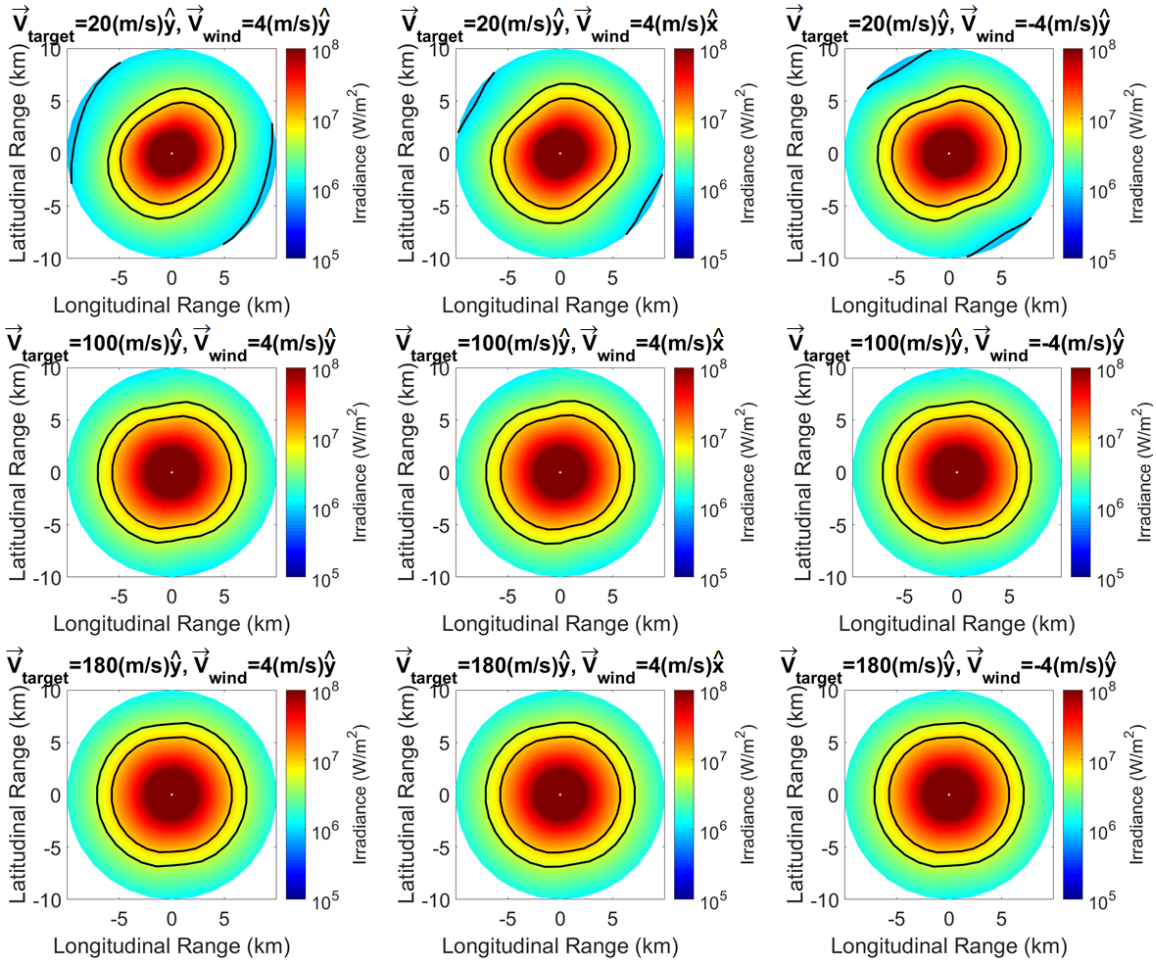

Figure 30. On-target irradiances for varying wind directions and target speeds, $\vec{V}_{ship} = -9(\mathrm{m/s})\hat{x}$, $P = 200$ kW and $H_T = 800$ m.

(2) The Effect of Wind Speed

In Figure 31, the on-target irradiances are plotted for constant laser output power, platform velocity and target height, which are $P = 200$ kW, $\vec{V}_{ship} = -9(\mathrm{m/s})\hat{x}$, and $H_T = 800$ m, respectively. Target speed changes from 20 m/s to 180 m/s in the y-direction and wind direction changes from 2 m/s to 8 m/s. As the target speed increases, it starts to dominate the irradiance pattern and the wind speed has less of an impact on the irradiance like the effect of platform speed.

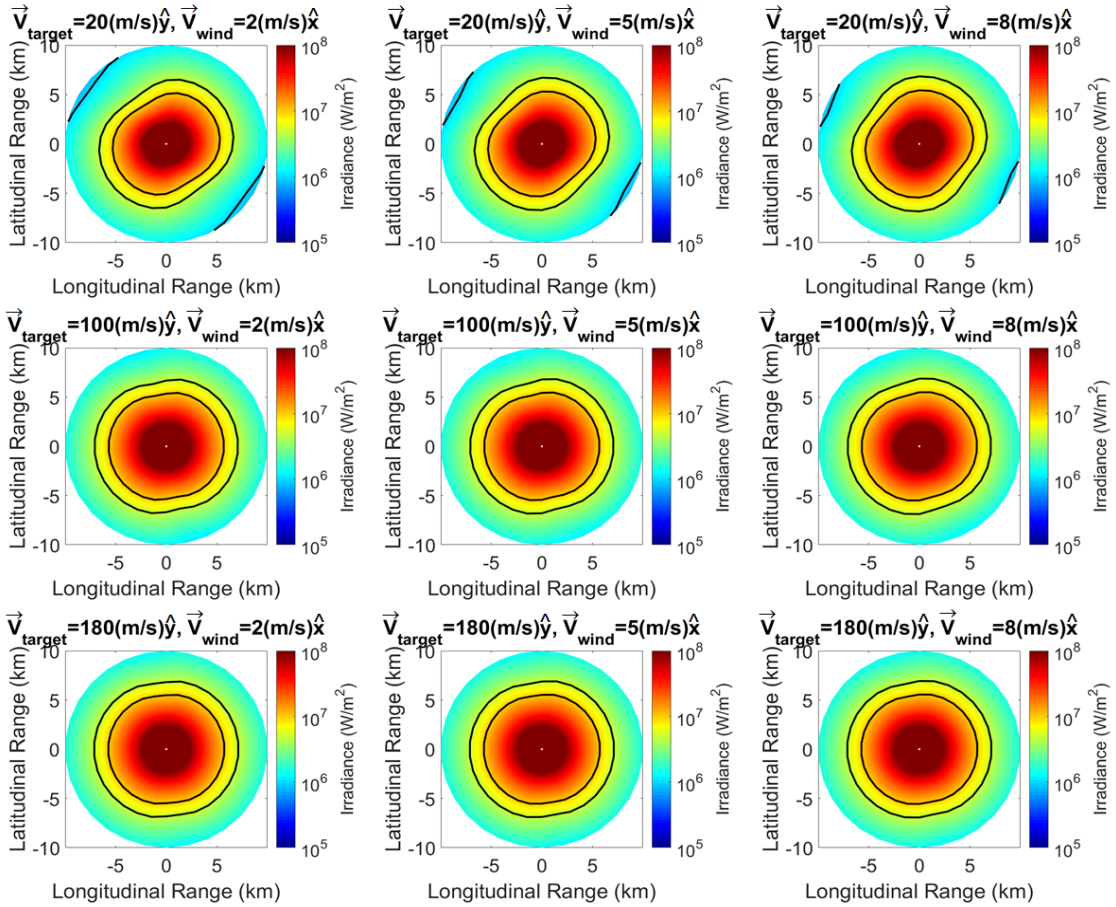

Figure 31. On-target irradiances for varying wind and target speeds, $\vec{V}_{ship} = -9(\mathrm{m/s})\hat{x}$, $P = 200\,\mathrm{kW}$ and $H_T = 800$ m.

2. Small Boat Target

In this sub-section, the on-target irradiances will be evaluated with varying target (small boat) velocities, varying platform (ship) velocities, varying wind velocities, varying laser output powers and constant boat height ($H_T = 0.4\,\mathrm{m}$).

a. The Effect of Target Velocity

The effect of relative target and platform motion on the atmospheric propagation will be studied with different target speeds and target headings.

(1) The Effect of Target Direction

In Figure 32, the on-target irradiances are plotted for constant wind velocity, platform velocity and target height, laser output power, and target speed, which are $\vec{V}_{wind} = -3(\mathrm{m/s})\hat{x}$, $\vec{V}_{ship} = 5(\mathrm{m/s})\hat{y}$, $H_T = 0.4\,\mathrm{m}$, $P = 200$ kW, and $V_{target} = 9$ m/s, respectively. The direction of the target changes for each plot. It is seen that the atmospheric propagation is affected in each plot with the change in target direction.

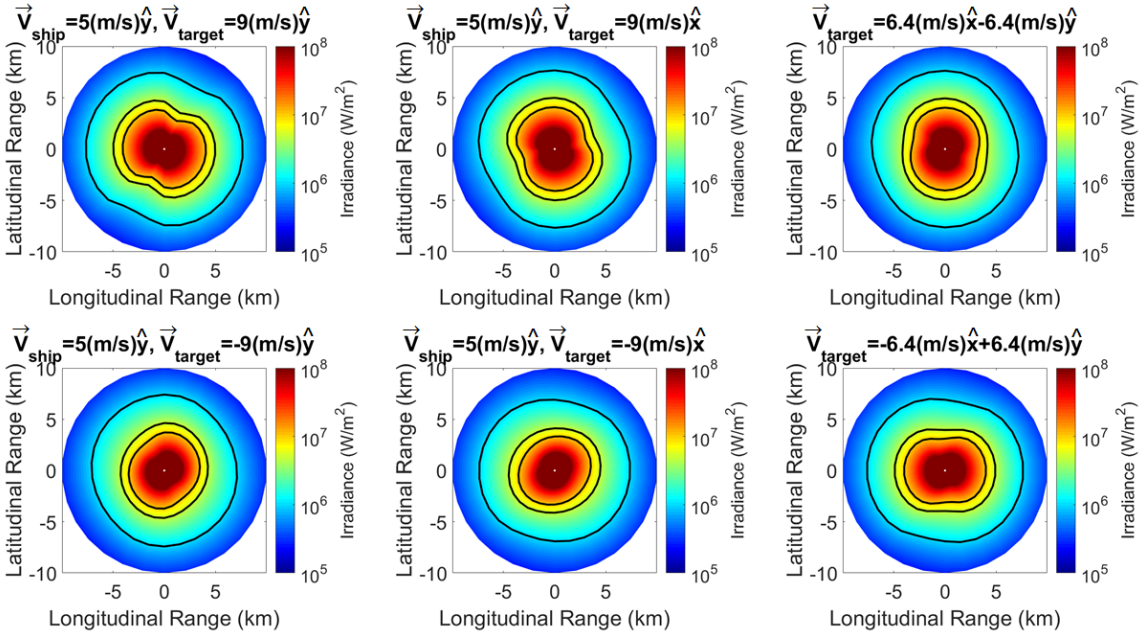

Figure 32. On-target irradiances for varying target directions, $\vec{V}_{wind} = -3(\mathrm{m/s})\hat{x}$, $\vec{V}_{ship} = 5(\mathrm{m/s})\hat{y}$, $P = 200\,\mathrm{kW}$, $V_{target} = 9$ m/s and $H_T = 0.4$ m.

(2) The Effect of Target Speed

In Figure 33, the on-target irradiances are plotted for constant laser output power, wind velocity, platform velocity and target height, which are $P = 200\,\mathrm{kW}$, $\vec{V}_{wind} = -3(\mathrm{m/s})\hat{x}$, $\vec{V}_{ship} = 5(\mathrm{m/s})\hat{y}$ and $H_T = 0.4\,\mathrm{m}$, respectively. Target speed changes from 0 m/s to 18 m/s in the x-direction. The on-target irradiance plot changes noticeably

until the target speed dominates the relative motion. After this speed, the change is very small.

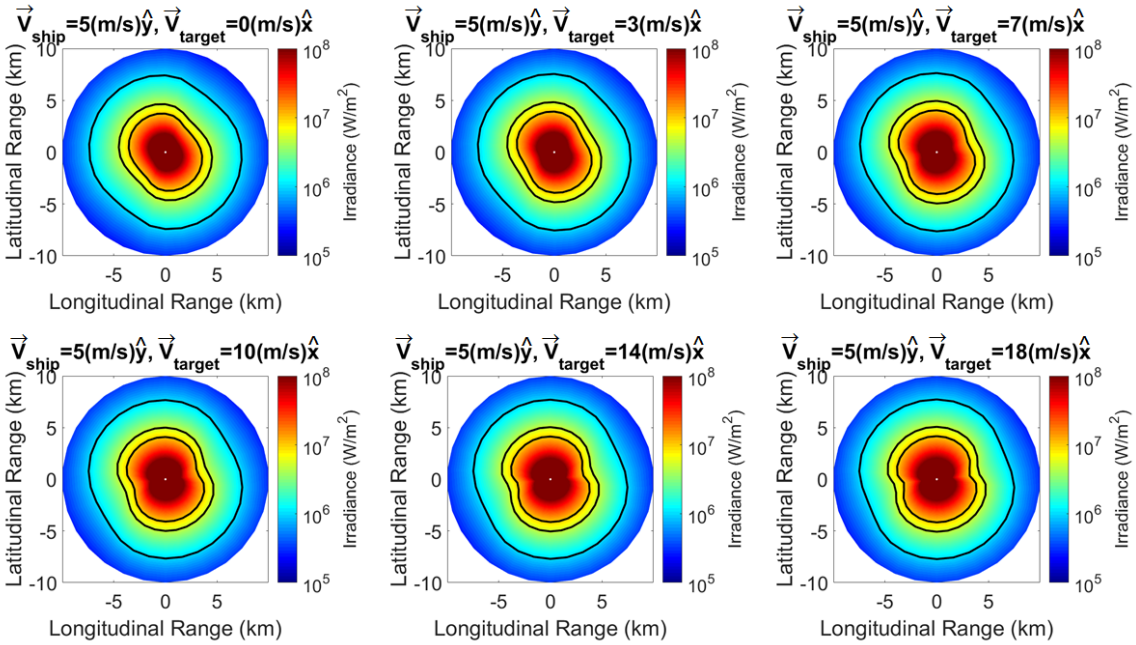

Figure 33. On-target irradiances for varying target velocities, $\vec{V}_{wind} = -3(\mathrm{m/s})\hat{x}$, $\vec{V}_{ship} = 5(\mathrm{m/s})\hat{y}$, $P = 200\,\mathrm{kW}$ and $H_T = 0.4$ m.

b. The Effect of Laser Output Power

In Figure 34, the on-target irradiances are plotted for constant wind velocity, platform velocity and target height, which are $\vec{V}_{wind} = -3(\mathrm{m/s})\hat{x}$, $\vec{V}_{ship} = 2(m/s)\hat{x} + 2(\mathrm{m/s})\hat{y}$ and $H_T = 0.4\,\mathrm{m}$, respectively. Target speed changes from 0 m/s to 18 m/s in the x-direction and laser output power changes from 200 kW to 1 MW. It is seen that the effect of the relative target and platform motion on the atmospheric propagation increases with the increase in the output laser power.

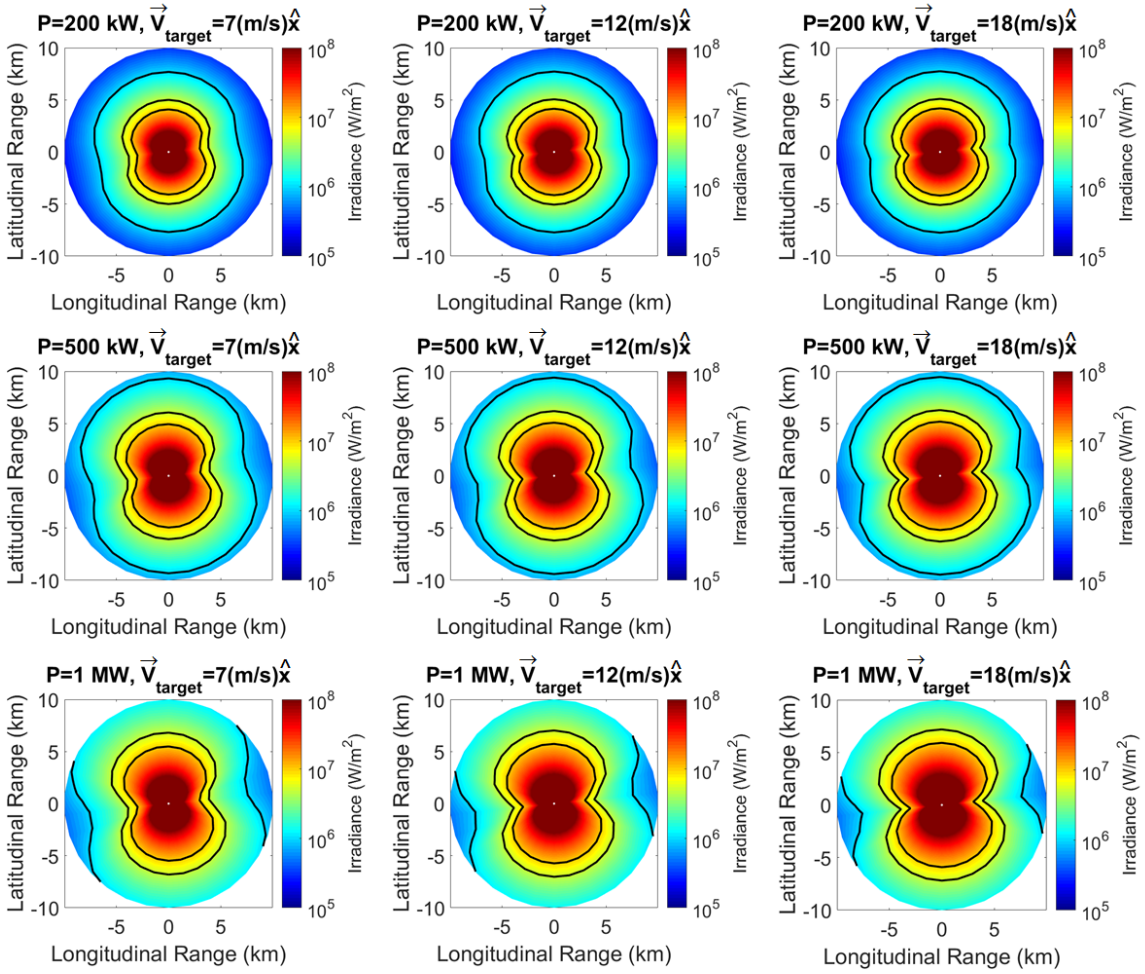

Figure 34. On-target irradiances for varying target velocities and laser output powers, $\vec{V}_{wind} = -3(\mathrm{m/s})\hat{x}$, $\vec{V}_{ship} = 2(m/s)\hat{x} + (\mathrm{m/s})\hat{y}$ and $H_T = 0.4$ m.

c. The Effect of Platform Velocity

The effect of the platform velocity on the effect of relative target and platform motion on the atmospheric propagation will be studied with different platform speeds and platform headings.

(1) The Effect of Platform Direction

In Figure 35, the on-target irradiances are plotted for constant laser output power, wind velocity and target height, which are $P = 200$ kW, $\vec{V}_{wind} = -3(\mathrm{m/s})\hat{x}$, and $H_T = 0.4$ m, respectively. Target speed changes from 7 m/s to 18 m/s in the y-direction and

platform direction changes but with a constant speed of 9 m/s. Unlike the UAV case, the target speed does not dominate the irradiance pattern since the difference between target and platform speed is not so large. As a result of this, the on-target irradiance pattern gets effected with any change in the platform heading, although this effect decreases as the target speed increases.

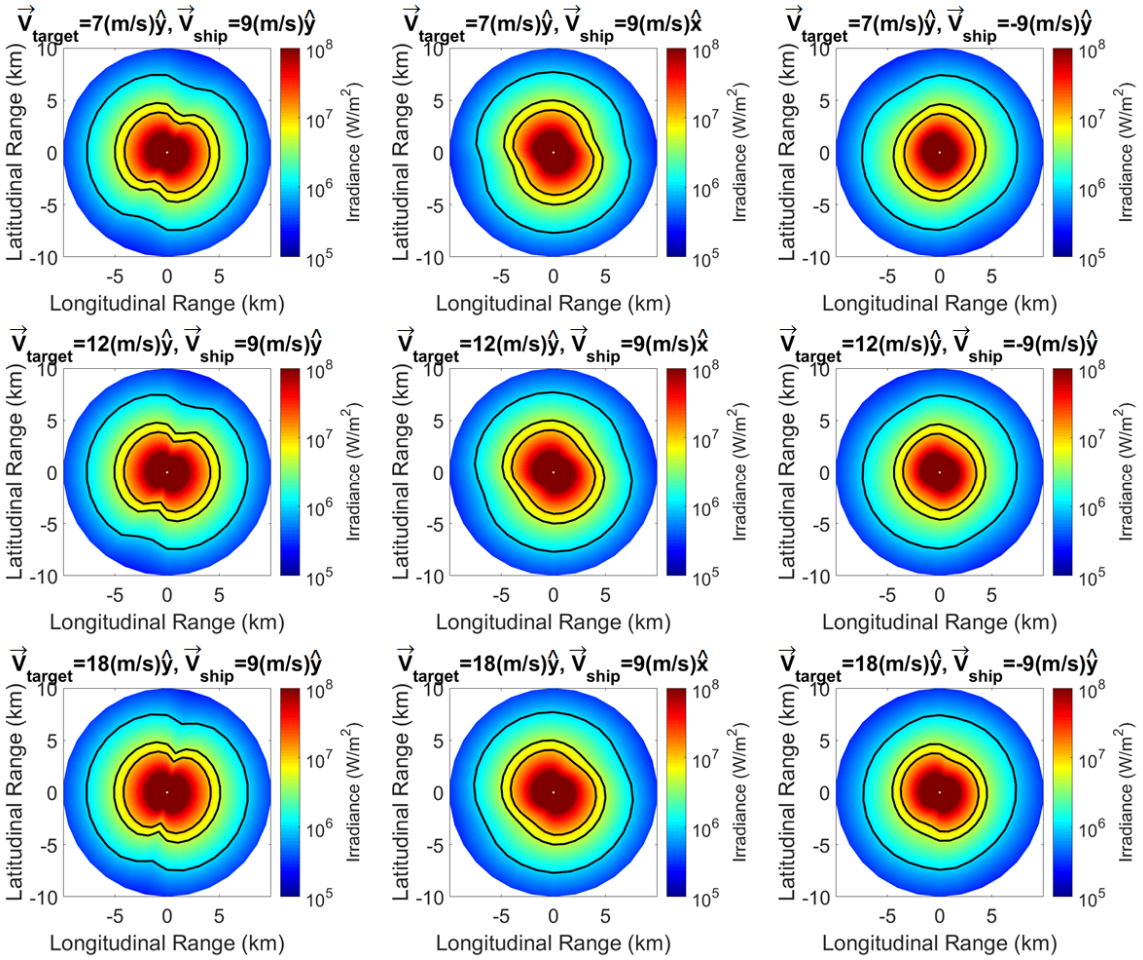

Figure 35. On-target irradiances for varying target speeds and platform headings, $\vec{V}_{wind} = -3(\mathrm{m/s})\hat{x}$, $P = 200\,\mathrm{kW}$ and $H_T = 0.4$ m.

(2) The Effect of Platform Speed

In Figure 36, the on-target irradiances are plotted for constant laser output power, wind velocity and target height, which are $P = 200\,\mathrm{kW}$, $\vec{V}_{wind} = -3(\mathrm{m/s})\hat{x}$, and $H_T = 0.4$

m, respectively. Target speed changes from 7 m/s to 18 m/s in the y-direction and platform speed changes from 5 m/s to 15 m/s. Unlike the UAV case, the target speed does not dominate the irradiance pattern since the difference between target and platform speed is not so large. As a result of this, the on-target irradiance pattern gets affected with any change in the platform speed, although this effect decreases as the target speed increases.

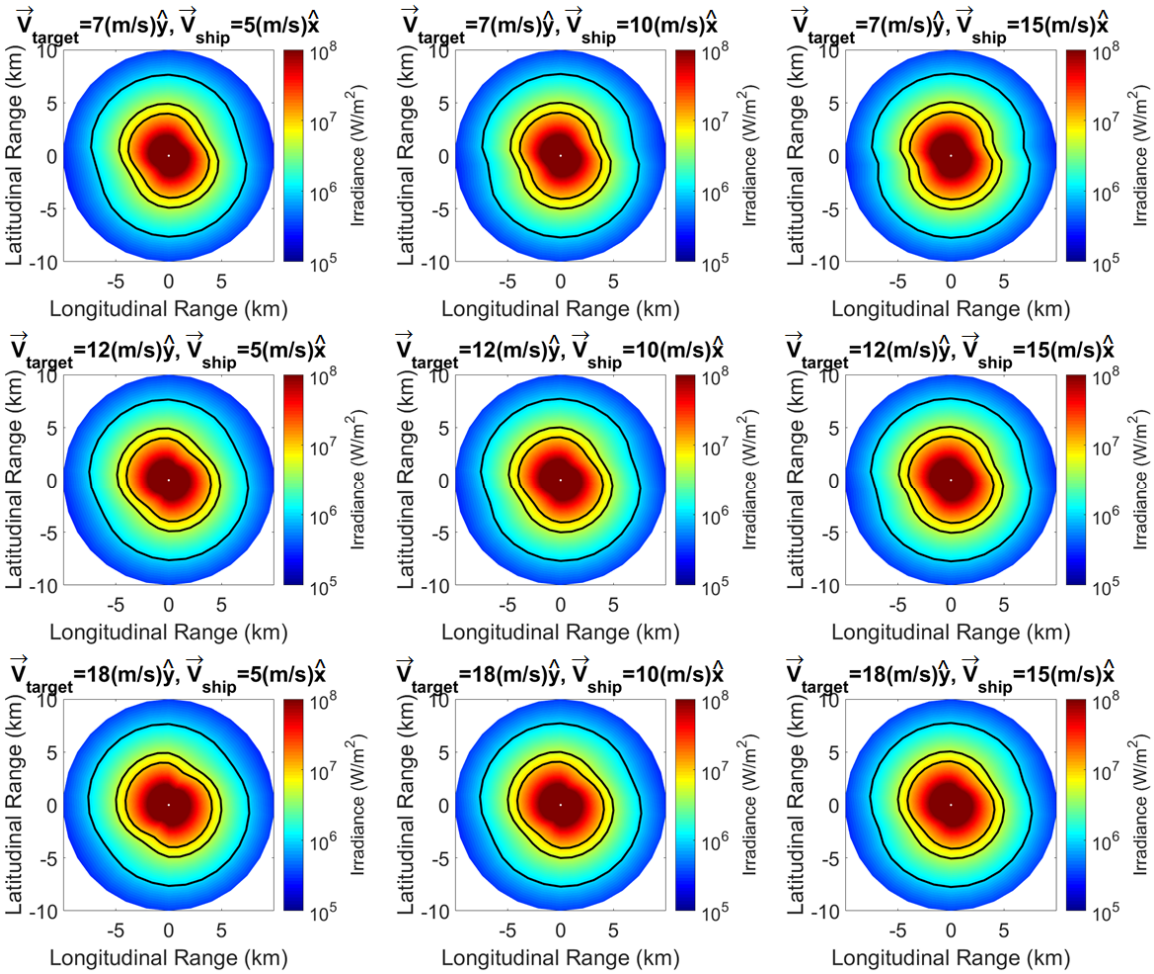

Figure 36. On-target irradiances for varying target and platform speeds, $\vec{V}_{wind} = -3(\mathrm{m/s})\hat{x}$, $P = 200\,\mathrm{kW}$ and $H_T = 0.4$ m.

d. The Effect of the Wind Velocity

The effect of the wind velocity on the atmospheric propagation will be studied with different wind speeds and headings.

(1) The Effect of Wind Direction

In Figure 37, the on-target irradiances are plotted for constant laser output power, platform velocity and target height, which are $P = 200\,\text{kW}$, $\vec{V}_{ship} = -3(\text{m/s})\hat{x}$, and $H_T = 0.4$ m, respectively. Target speed changes from 7 m/s to 18 m/s in the y-direction and wind direction changes but with a constant speed of 7 m/s. Unlike the UAV case, the target speed does not dominate the irradiance pattern since the difference between target and wind speed is not so large. As a result of this, the on-target irradiance pattern gets affected with any change in the wind heading, although this effect decreases as the target speed increases.

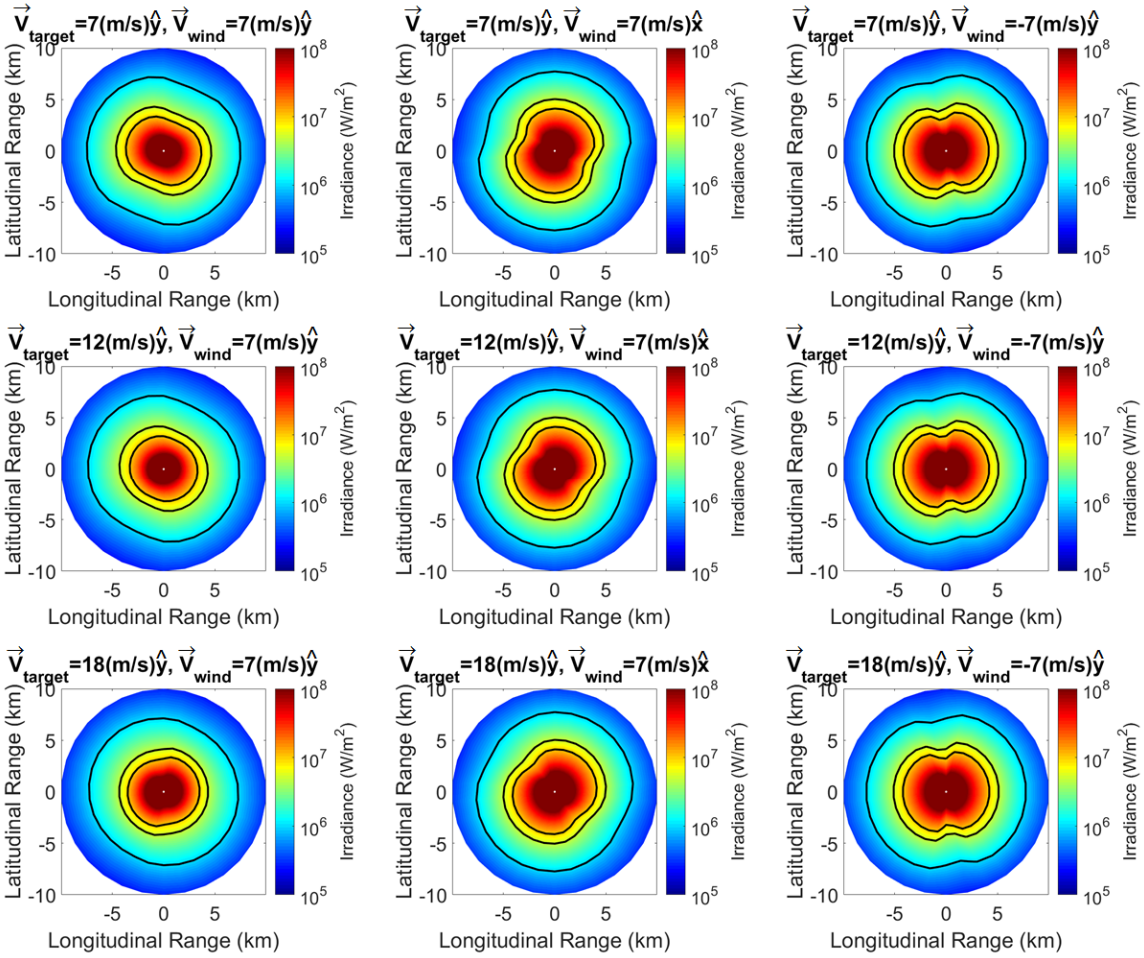

Figure 37. On-target irradiances for varying target speeds and wind headings, $\vec{V}_{ship} = -3(\mathrm{m/s})\hat{x}$, $P = 200\,\mathrm{kW}$ and $H_T = 0.4$ m.

(2) The Effect of Wind Speed

In Figure 38, the on-target irradiances are plotted for constant laser output power, platform velocity and target height, which are $P = 200\,\mathrm{kW}$, $\vec{V}_{ship} = -3(\mathrm{m/s})\hat{x}$, and $H_T = 0.4$ m, respectively. Target speed changes from 7 m/s to 18 m/s in the y-direction and wind speed changes from 0 m/s to 10 m/s. Unlike the UAV case, the target speed does not dominate the irradiance pattern since the difference between target and wind speed is not so large. As a result of this, the on-target irradiance pattern gets affected with any change in the wind speed, although this effect decreases as the target speed increases.

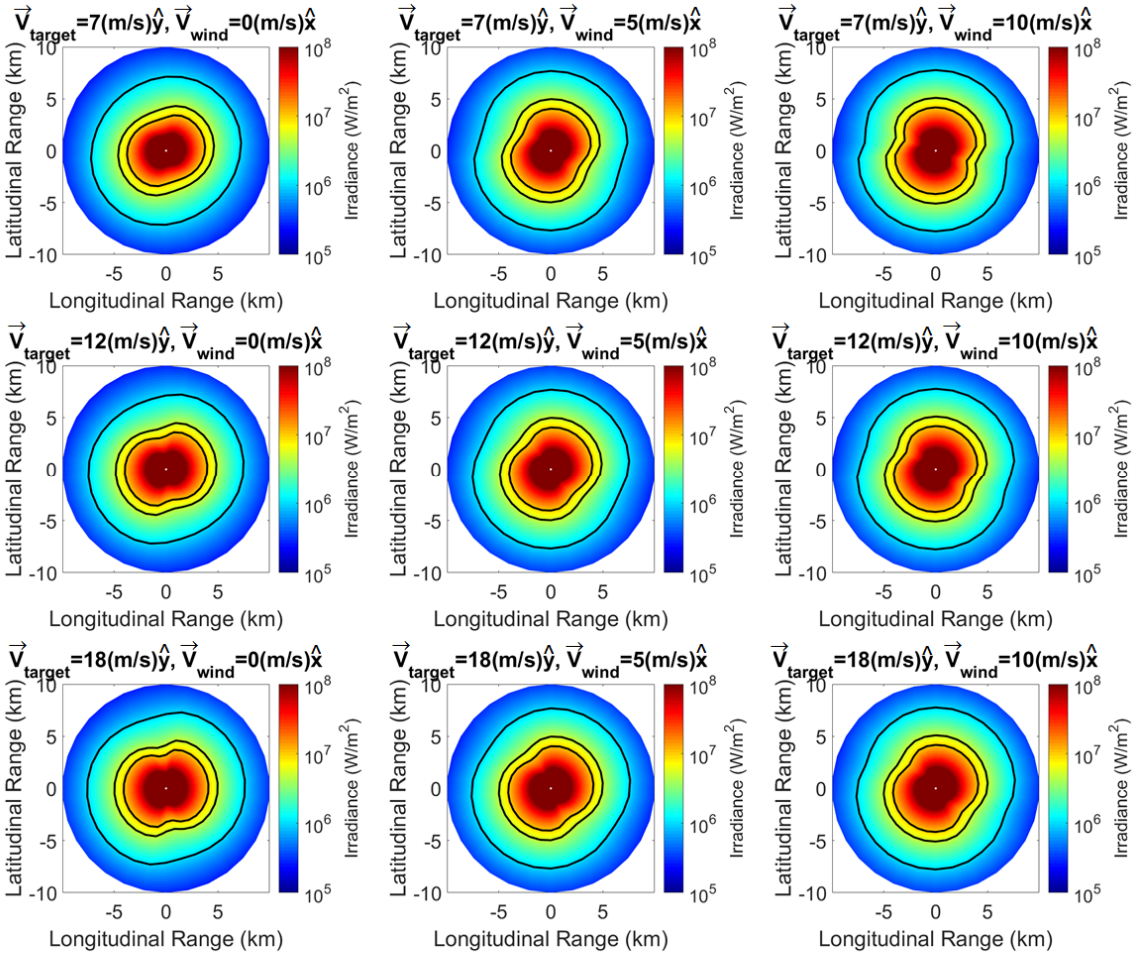

Figure 38. On-target irradiances for varying target and wind speeds, $\vec{V}_{ship} = -3(\mathrm{m/s})\hat{x}$, $P = 200\,\mathrm{kW}$ and $H_T = 0.4$ m.

VI. CONCLUSIONS

According to the results, the effects of relative target and platform motion on the atmospheric propagation of HELs depend on parameters like target altitude, target velocity, platform velocity, laser output power, and wind velocity. As the target altitude increases, the effect of the relative motion on the propagation decreases, because the slew rate of the beam director decreases with the increase in target altitude. The wind velocity can either decrease or increase the relative motion effect on propagation for a specific target acquisition, depending on the specific velocities of the platform and target as well as their relative positions. As an example, as the target speed becomes faster than the platform speed, the relative motion becomes dominated by the target speed. Changes in both target and platform direction affect the propagation of the laser regardless of the target altitude, target and platform speeds, and the wind velocity, because the effective cross wind changes with the change in directions for each case. The effect of the relative target and platform motion on the atmospheric propagation also depends on the output laser power, since target/platform motion mainly affects thermal blooming, which is more prevalent at higher output laser powers.

As a result, the relative target and platform motion significantly affects the atmospheric propagation of HELs, and the level that the propagation is affected depends on the parameters discussed above. HELs can be used more effectively by the users considering these effects.

THIS PAGE INTENTIONALLY LEFT BLANK

LIST OF REFERENCES

[1] G. P. Perram et al., *Introduction to Laser Weapon Systems*, 1st ed. Albuquerque, NM: Directed Energy Professional Society, 2010.

[2] Maritime laser demonstration. Northrop Grumman. [Online]. Available: http://www.northropgrumman.com/Capabilities/SolidStateHighEnergyLaserSystems/Pages/MaritimeLaserDemonstration.aspx. [Accessed: 31- Mar- 2016].

[3] B. L Thompson, "Directed energy weapons: Technologies, applications, and implications," *Lexington Institute White Paper*, Feb. 2003. [Online]. Available: http://lexingtoninstitute.org/wp-content/uploads/directed-energy-weapons.pdf. [Accessed: 31- Mar- 2016].

[4] R. O'Rourke, "Navy shipboard lasers for surface, air, and missile defense: Background and issues for Congress," *Congressional Research Service*, Mar. 2013.

[5] K. N. Liou, *An Introduction to Atmospheric Radiation*, 2nd ed. San Diego, CA: Academic Press, 2002.

[6] R. Hudson, *Infrared System Engineering*, New York: Wiley-Interscience, 1969.

[7] F. G. Gebhardt, "High power laser propagation," *Applied Optics*, vol. 15, no. 6, Jun. 1976.

[8] R. McClatchey and J. Selby, *Atmospheric Attenuation of Laser Radiation from 0.76 to 31.25 [sign for micron] m*, Bedford, MA: Air Force Cambridge Research Laboratories, 1974.

[9] H. Weichel, *Laser Beam Propagation in the Atmosphere*, Bellingham, WA: SPIE Optical Engineering Press, 1990.

[10] WaveTrain software. Image generated by Dr. Conor Pogue, Physics Department, Naval Postgraduate School, Feb 2016.

[11] F. G. Gebhardt, "Twenty-five years of thermal blooming: An overview," *SPIE Proceedings*, vol. 1221, May 1990.

[12] A. E. Siegman, "How to (maybe) measure laser beam quality," *Diode Pumped Solid State Lasers: Applications and Issues*, Stanford Univ., Oct. 1997.

[13] H. Yura, "Atmospheric turbulence induced laser beam spread," *Appl. Opt.*, vol. 10, no. 12, p. 2771, 1971.

[14] C. R. Fussman, “High energy laser propagation in various atmospheric conditions, utilizing a new, accelerated scaling code,” M.S. thesis, Physics Dept., Naval Postgraduate School, Monterey,CA, 2014.

[15] M. Alvarez, “Feasibility of high energy laser weapons onboard USMC attack helicopters,” M.S. thesis, Physics Dept., Naval Postgraduate School, Monterey, CA, 2013.

[16] Modtran5.com, MODTRAN®5: Narrow band model atmospheric radiative transfer code, 2016. [Online]. Available: http://modtran5.com/. [Accessed: 01-Mar- 2016].

[17] S. Coy. (2013). *WaveTrain: A user-friendly wave optics propagation code* [Online]. Available: https://www.mza.com/publications/wtspiepaper.htm.

INITIAL DISTRIBUTION LIST

1. Defense Technical Information Center
   Ft. Belvoir, Virginia

2. Dudley Knox Library
   Naval Postgraduate School
   Monterey, California